



Research article

Optimizing optical thermometry with tri-doped Ba₂GdV₃O₁₁ phosphors: Ratiometric and fluorescence lifetime analysis

Ikhlas Kachou^a, Kamel Saidi^a, Utku Ekim^b, Mohamed Dammak^{a,*}, Miray Çelikbilek Ersundu^b, Ali Erçin Ersundu^{b,**}

^a Laboratoire de Physique Appliquée, Groupe de Physique des Matériaux Luminescents, Faculté des Sciences de Sfax, Département de Physique, Université de Sfax, BP 1171, Sfax, Tunisia

^b Yıldız Technical University, Faculty of Chemical and Metallurgical Engineering, Department of Metallurgical and Materials Engineering, Glass Research and Development Laboratory, Istanbul, 34220, Türkiye

ARTICLE INFO

Keywords:

Optical temperature sensing
Upconversion luminescence
FIR
Fluorescence lifetime

ABSTRACT

Optical sensor technology has undergone a transformative evolution with the advent of fluorescence ratio techniques (FIR) and fluorescence lifetime (FL) strategies, revolutionizing precision, performance, and reliability. This study delves into the synthesis of Ba₂GdV₃O₁₁ phosphors doped with Ho³⁺/Nd³⁺, Er³⁺, and Yb³⁺, employing the sol-gel method for upconverting material fabrication. A thorough investigation into the structural, morphological, and optical properties of the synthesized phosphors is conducted. Excitation at 980 nm unveils upconversion (UC) emissions across green and red spectra. The intensities of the observed emission bands for Ho³⁺, Nd³⁺, and Er³⁺ demonstrate significant sensitivity to fluctuations in temperature. Temperature sensing relies on the ⁴S_{3/2} and ²H_{11/2} upconversion emissions bands, in addition to the emission lifetimes at ⁴S_{3/2}. Enhanced thermal sensitivity values are attained, reaching up to 1.03 % K⁻¹ and 1.07 % K⁻¹ using the FIR strategy, and up to 0.146 % K⁻¹ and 0.47 % K⁻¹ with the FL strategy for Ho³⁺/Er³⁺/Yb³⁺ and Nd³⁺/Er³⁺/Yb³⁺ tri-doped Ba₂GdV₃O₁₁ phosphors, respectively. Furthermore, the studied phosphors exhibit remarkable precision in detecting minute temperature changes (0.3 K), positioning them as promising candidates for precise temperature sensing. This study pioneers innovative methodologies to advance optical thermometry techniques, offering promising prospects for scientific and industrial applications reliant on precise optical temperature sensing.

1. Introduction

The fascinating field of upconverting materials featuring rare earth (RE) dopants has attracted significant research attention due to their considerable potential across various applications such as displays, temperature sensors, solar cells, bio-imaging, fingerprint detection, and optoelectronic devices [1–4]. However, it is the realm of temperature sensors based on RE-doped UC phosphors that has particularly captivated the scientific community. These sensors present unique benefits, such as swift response times, electromagnetic passivity, and exceptional thermal sensitivity [5,6].

Inorganic materials infused with rare earth (RE) elements have risen as the favored choice for demonstrating near-infrared (NIR) to

* Corresponding author.

** Corresponding author.

E-mail addresses: madidammak@yahoo.fr (M. Dammak), ersundu@yildiz.edu.tr (A. Erçin Ersundu).

<https://doi.org/10.1016/j.heliyon.2024.e30062>

Received 18 January 2024; Received in revised form 18 April 2024; Accepted 18 April 2024

Available online 24 April 2024

2405-8440/© 2024 Published by Elsevier Ltd.

This is an open access article under the CC BY-NC-ND license

(<http://creativecommons.org/licenses/by-nc-nd/4.0/>).

visible upconversion or NIR-to-NIR down-shifting occurrences. This inclination is grounded in several advantageous factors, including the availability of host materials with low maximum phonon energy, as well as the feasibility and effectiveness of energy transfer and frequency conversion among the rare earth ions [7]. Trivalent rare earth (RE) ions, including Er^{3+} , Ho^{3+} , Tm^{3+} , and Tb^{3+} , are prominently chosen as the primary luminescent activators frequently utilized in upconversion processes [8]. To enhance the emission intensity, Yb^{3+} is often co-doped, leveraging its high absorption cross-section in the near-infrared (NIR) range [9].

The fluorescence ratio technique (FIR) stands as the prevailing method in optical thermometry, providing swift measurements, superior precision, and high resolution. This technique primarily hinges on upconversion luminescence (UCL), with the excitation wavelength typically centered around 980 nm, as documented in various studies [10]. Conversely, the fluorescence lifetime (FL) sensing method involves measuring the lifetimes of luminescent energy levels within the temperature range under investigation. Both FIR thermometry and FL thermometry stand as valuable techniques in temperature measurement, each presenting distinct advantages and limitations. FIR thermometry, which relies on calculating fluorescence intensity ratios, has demonstrated rapid and precise results, as evidenced by previous studies [11,12]. On the other hand, FL thermometry involves measuring the lifetimes of luminescent energy levels across the temperature range under examination. This approach offers the benefit of integrating a time-based encoding system, which remains unaffected by external factors such as changes in coupling degree, optical fiber transmission efficiency, and fluctuations in excitation light intensity. The selection between FIR and FL thermometry hinges on various factors, including specific measurement prerequisites, properties of the material under scrutiny, the targeted level of accuracy, and the required speed in temperature sensing [13]. By considering these factors, researchers can select the most appropriate thermometric technique for their particular application.

Temperature-sensitive materials doped with rare earth (RE) elements are utilized in luminescent thermometry techniques, capitalizing on the energy transfer between the sensitizer Yb^{3+} and various lanthanide ions (such as Er^{3+} , Ho^{3+} , Tb^{3+} , Nd^{3+} , and Tm^{3+}), acting as photoluminescence (PL) activators in near-infrared (NIR) activated upconversion (UC) systems. The interaction among these ions constitutes the fundamental mechanism governing the operation of the upconversion system [14–16]. Unlike luminescent quantum dots that contain heavy metals [17–19], phosphors doped with rare earth (RE) ions exhibit considerable potential for biological applications owing to their reduced cytotoxicity. Most research articles in the field primarily focus on investigating the thermometric properties of individual luminescent centers, such as Er^{3+} , Ho^{3+} , Tm^{3+} , and Pr^{3+} [20–22]. However, the presence of a second center in co-doped compounds can significantly alter their thermometric properties. This phenomenon arises from the potential energy transfer between the two ions, which directly influences the population of emitting energy levels and, consequently, the luminescent behavior, particularly at elevated temperatures. Notably, pairs of lanthanide ions $\text{Ho}^{3+}/\text{Er}^{3+}$ and $\text{Nd}^{3+}/\text{Er}^{3+}$ exhibit emissions in the green spectral range (520 nm–560 nm), meanwhile, Ho^{3+} and Er^{3+} ions also emit in the red range, typically around 650 nm. Hence, the objective of this investigation is to examine the impact of $\text{Ho}^{3+}/\text{Er}^{3+}$ and $\text{Nd}^{3+}/\text{Er}^{3+}$ co-dopants on the thermometric properties. Furthermore, the thermometric approach based on fluorescence lifetime (FL) will be affected by the energy transfer between Er^{3+} and Ho^{3+} , as well as Nd^{3+} ions. This energy transfer induces alterations in the thermometric parameters, consequently influencing the precision and dependability of the FL thermometric strategy. Materials hosting lower phonon energy are highly sought after, as they enhance upconversion (UC) efficiency by suppressing multi-photon relaxation processes. Inorganic matrices characterized by low phonon energy, including fluorides, oxides, vanadates, phosphates, and borates, are commonly utilized to incorporate upconversion dopants, effectively minimizing undesired multi-phonon relaxation [23–26]. These matrices demonstrate excellent performance as phosphors due to their thermal stability and low phonon energies [27]. $\text{Ba}_2\text{GdV}_3\text{O}_{11}$ stands out as a highly esteemed host material among them, attributed to its capacity to endure high-temperature processing, compatibility with various lanthanide ions as co-dopants, ease of synthesis at elevated temperatures, and capability to exhibit self-activated luminescence. According to the findings from previous studies, $\text{Ba}_2\text{GdV}_3\text{O}_{11}$ has been subject to doping with a range of lanthanide ions. These include Sm^{3+} , Eu^{3+} , Dy^{3+} , $\text{Yb}^{3+}/\text{Ln}^{3+}$ (where Ln^{3+} represents Er^{3+} , Ho^{3+} , Tm^{3+}), and Er^{3+} [28–32].

Thus, the main focus of this study revolves around analyzing the $\text{Ba}_2\text{GdV}_3\text{O}_{11}$ host material tri-doped with $\text{Ho}^{3+}/\text{Er}^{3+}/\text{Yb}^{3+}$ and $\text{Nd}^{3+}/\text{Er}^{3+}/\text{Yb}^{3+}$ rare earth (RE) ions. The primary emphasis lies in examining its strong green upconversion (UC) emission properties, which are activated under 980 nm laser excitation, within the temperature range of 298–573 K. The detailed discussion delves into the temperature sensing characteristics utilizing the fluorescence intensity ratio (FIR) technique. Furthermore, an investigation into the fluorescence (FL) of the green emission under 980 nm.

2. Experimental studies

2.1. Synthesis of $\text{Ho}^{3+}/\text{Nd}^{3+}$, Er^{3+} , Yb^{3+} tri-doped $\text{Ba}_2\text{GdV}_3\text{O}_{11}$ phosphors

In the synthesis procedure, $\text{Ba}_2\text{GdV}_3\text{O}_{11}$ phosphors tri-doped with $\text{Ho}^{3+}/\text{Er}^{3+}/\text{Yb}^{3+}$ and $\text{Nd}^{3+}/\text{Er}^{3+}/\text{Yb}^{3+}$ are prepared utilizing the citric acid sol-gel cycle. All chemicals employed, including barium nitrate [$\text{Ba}(\text{NO}_3)_2$ (99.0 %)], gadolinium nitrate hexahydrate [$\text{Gd}(\text{NO}_3)_3 \cdot 6\text{H}_2\text{O}$ (99.9 %)], ammonium metavanadate [NH_4VO_3 (99.96 %)], holmium nitrate pentahydrate [$\text{Ho}(\text{NO}_3)_3 \cdot 5\text{H}_2\text{O}$ (99.9 %)], neodymium nitrate hexahydrate [$\text{Nd}(\text{NO}_3)_3 \cdot 6\text{H}_2\text{O}$], erbium nitrate pentahydrate [($\text{Er}(\text{NO}_3)_3 \cdot 5\text{H}_2\text{O}$ (99.9 %)], ytterbium nitrate pentahydrate [$\text{Yb}(\text{NO}_3)_3 \cdot 5\text{H}_2\text{O}$ (99.9 %)] and citric acid [$\text{C}_6\text{H}_8\text{O}_7$ (99.0 %)], are procured from Sigma-Aldrich and used directly without further purification. The synthesis method involves combining all precursors in an Erlenmeyer flask and stirring magnetically at 70 °C. Following this, citric acid is introduced, leading to a color change from green to blue. The solution is then swirled and heated to 80 °C until it hydrolyzes into a sol and forms a gel. The resulting xerogel is annealed at 400 °C for 3 h, yielding black-colored flakes. Finally, the gel undergoes calcination at 700 °C for approximately 4 h to yield pure-phase crystals. This approach is utilized to fabricate $\text{Ba}_2\text{GdV}_3\text{O}_{11}$ nanostructures doped with specific ion concentrations: 1 % $\text{Ho}^{3+}/2$ % $\text{Er}^{3+}/15$ % Yb^{3+} and 1 % $\text{Nd}^{3+}/2$ % $\text{Er}^{3+}/15$ % Yb^{3+} . These concentrations are selected to prevent the quenching of upconversion (UC) luminescence, aligning with prior research

findings and supported by both established theoretical understanding and experimental data [33]. Notably, in UC systems, a prevalent approach in the literature involves employing a higher proportion of sensitizer (Yb^{3+}) alongside lower concentrations of emitters (Ho^{3+} , Nd^{3+} , and Er^{3+}), as this combination has proven effective in generating strong emissions [31,34].

2.2. Characterization studies

The synthesized phosphors are subjected to analysis within the 2θ range spanning from 10 to 80° using a Bruker AXS D8 X-ray diffractometer from Germany. $\text{Cu K}\alpha$ radiation (1.5406 \AA) is utilized with a step size of 0.015° . The instrument operates at 40 kV and 30 mA for phase detection. A comparison of XRD peak positions and intensities with the JCPDS card files is conducted to verify the crystallized phases.

Morphological examination is performed using a Thermo Scientific Apreo 2 S LoVac field emission scanning electron microscope (FE-SEM). UV–Vis–NIR absorption measurements are carried out with a UV–Vis–NIR spectrometer (PerkinElmer Lambda 950).

For steady-state and time-resolved photoluminescence (PL) properties, an Edinburgh Instruments FS5 spectrofluorometer is employed at equilibrium and temporal resolution. PL spectra are recorded with a laser diode emitting at 980 nm , ensuring a signal-to-noise ratio of the Raman signal of water surpassing $6000:1$ and a spectral resolution of 0.5 nm , using an excitation power of 0.5 W .

The temperature dependence of the PL properties is explored using a Pike Technologies solid-state transmission accessory integrated into the spectrofluorometer. This enables measurements across a temperature range spanning from 298 K to 573 K . To ensure precise temperature assessments, a calibration curve is established correlating the optical signal (such as fluorescence intensity or lifetime) with temperature. This is performed under the lowest laser power setting that still allows for reliable signal detection.

A controlled and stable measurement environment is meticulously maintained. Prior to any laser excitation, baseline measurements are taken to determine the intrinsic temperature of the sample under the specific experimental conditions. Throughout the temperature measurements, continuous monitoring of both the laser power and sample temperature is conducted. Additionally, the calibration curve is regularly validated by assessing known temperatures using an independent reference thermometer, ensuring the accuracy and reliability of the measurements.

The influence of laser-induced heating is taken into account during subsequent data analysis, with corrections applied as necessary. This involves subtracting the baseline temperature from the recorded temperature to reveal the actual temperature change induced by the laser. Furthermore, a thorough validation of the temperature measurement protocol is conducted, covering various conditions and sample types. This meticulous assessment plays a crucial role in demonstrating the protocol's versatility and accuracy across diverse experimental scenarios.

Time-resolved photoluminescence (PL) spectra are obtained using a 980 nm pulsed laser operating at a frequency of 1 kHz . This is carried out to measure the characteristic lifetime of Er^{3+} emissions at 555 and 550 nm ($^4\text{S}_{3/2}$ level) for $\text{Ho}^{3+}/\text{Er}^{3+}/\text{Yb}^{3+}$ and $\text{Nd}^{3+}/\text{Er}^{3+}/\text{Yb}^{3+}$ tri-doped $\text{Ba}_2\text{GdV}_3\text{O}_{11}$ phosphors at different temperatures.

3. Results and discussion

3.1. Crystal structure, morphology and optical properties

The crystal structure of the synthesized $\text{Ho}^{3+}/\text{Er}^{3+}/\text{Yb}^{3+}$ and $\text{Nd}^{3+}/\text{Er}^{3+}/\text{Yb}^{3+}$ tri-doped $\text{Ba}_2\text{GdV}_3\text{O}_{11}$ phosphors is determined using the powder XRD technique (Fig. S1). Fig. 1(a) and (b) depict the Rietveld refinement of XRD data for $\text{Ho}^{3+}/\text{Er}^{3+}/\text{Yb}^{3+}$ and $\text{Nd}^{3+}/\text{Er}^{3+}/\text{Yb}^{3+}$ tri-doped $\text{Ba}_2\text{GdV}_3\text{O}_{11}$ phosphors, respectively. The diffraction peak patterns correspond to the JCPDS card number 45-0097, indicating that the insertion of $\text{Ho}^{3+}/\text{Nd}^{3+}$, Er^{3+} , and Yb^{3+} does not significantly alter the phase pattern.

The Rietveld data fit, conducted using the FullProf Suite program, reveals that the synthesized $\text{Ba}_2\text{GdV}_3\text{O}_{11}$ crystallizes into a monoclinic crystal structure with $P2_1/c$ space group symmetry. The unit cell parameters for $\text{Ho}^{3+}/\text{Er}^{3+}/\text{Yb}^{3+}$ tri-doped $\text{Ba}_2\text{GdV}_3\text{O}_{11}$

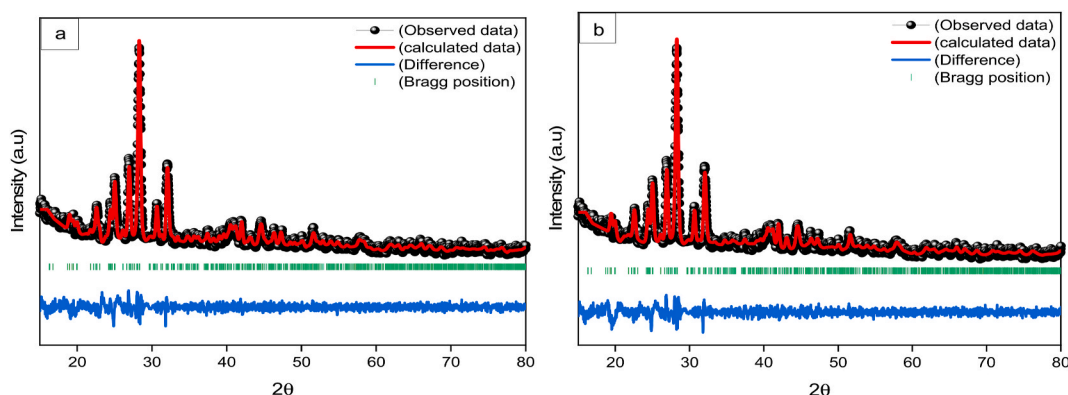


Fig. 1. Rietveld refinement of XRD data for (a) $\text{Ho}^{3+}/\text{Er}^{3+}/\text{Yb}^{3+}$ tri-doped $\text{Ba}_2\text{GdV}_3\text{O}_{11}$ phosphors: $\chi^2 = 1.10$, $R_{\text{wp}} = 12.87$, (b) $\text{Nd}^{3+}/\text{Er}^{3+}/\text{Yb}^{3+}$ tri-doped $\text{Ba}_2\text{GdV}_3\text{O}_{11}$ phosphors: $\chi^2 = 1.12$, $R_{\text{wp}} = 12.68$ tri-doped $\text{Ba}_2\text{GdV}_3\text{O}_{11}$ phosphors.

phosphors are determined to be $a = 12.36107 \text{ \AA}$, $b = 7.73535 \text{ \AA}$, $c = 11.17577 \text{ \AA}$, $\alpha = 90^\circ$, $\beta = 103.53646^\circ$, $\gamma = 90^\circ$, and $V = 1048.21 \text{ \AA}^3$, while for $\text{Nd}^{3+}/\text{Er}^{3+}/\text{Yb}^{3+}$ tri-doped $\text{Ba}_2\text{GdV}_3\text{O}_{11}$ phosphors, the unit cell dimensions are calculated to be $a = 12.37275 \text{ \AA}$, $b = 7.735513 \text{ \AA}$, $c = 11.1819 \text{ \AA}$, $\alpha = 90^\circ$, $\beta = 103.55934^\circ$, $\gamma = 90^\circ$, and $V = 1048.21 \text{ \AA}^3$, with four formula units in each unit cell [28,32].

Fig. 2(a) and (b) display representative FE-SEM images depicting the morphological properties and grain size distribution of $\text{Ho}^{3+}/\text{Er}^{3+}/\text{Yb}^{3+}$ and $\text{Nd}^{3+}/\text{Er}^{3+}/\text{Yb}^{3+}$ tri-doped $\text{Ba}_2\text{GdV}_3\text{O}_{11}$ phosphors, respectively. The images obtained offer clear evidence of the successful synthesis of $\text{Ho}^{3+}/\text{Er}^{3+}/\text{Yb}^{3+}$ and $\text{Nd}^{3+}/\text{Er}^{3+}/\text{Yb}^{3+}$ tri-doped $\text{Ba}_2\text{GdV}_3\text{O}_{11}$ particles at the nanoscale, with sizes ranging between 100 and 300 nm. However, it is important to note that the sol-gel synthesis method employed in this process leads to particle agglomeration, resulting in densely packed particles with irregular shapes, attributed to the high surface energy of the particles. Despite the particle agglomeration, the densely packed nanoparticles contribute to a reduction in light scattering, thereby enhancing the luminous intensity. Consequently, the resulting $\text{Ho}^{3+}/\text{Er}^{3+}/\text{Yb}^{3+}$ and $\text{Nd}^{3+}/\text{Er}^{3+}/\text{Yb}^{3+}$ tri-doped $\text{Ba}_2\text{GdV}_3\text{O}_{11}$ phosphors exhibit well-crystallized structures and possess remarkable luminescence properties, characterized by strong and vibrant emission.

Fig. 3(a) depicts the diffuse reflectance spectrum of $\text{Ho}^{3+}/\text{Er}^{3+}/\text{Yb}^{3+}$ tri-doped $\text{Ba}_2\text{GdV}_3\text{O}_{11}$ phosphors across the UV-VIS-NIR spectral range. Notably, the phosphors exhibit significant UV absorption attributed to the $\text{O}^{2-} \rightarrow \text{V}^{5+}$ charge transfer transition in the VO_4^{3-} group [35]. Three distinct absorption bands emerge at 525, 545, and 655 nm, associated with the ${}^2\text{H}_{11/2} \rightarrow {}^4\text{I}_{15/2}$ (Er^{3+}), ${}^5\text{S}_2/{}^5\text{F}_4 \rightarrow {}^5\text{I}_8$ (Ho^{3+}) + ${}^4\text{S}_{3/2} \rightarrow {}^4\text{I}_{15/2}$ (Er^{3+}), and ${}^5\text{F}_5 \rightarrow {}^5\text{I}_8$ (Ho^{3+}) + ${}^4\text{F}_{9/2} \rightarrow {}^4\text{I}_{15/2}$ (Er^{3+}) transitions, respectively [27,36]. Furthermore, a robust absorption band centered at 980 nm is observed, ascribed to the ${}^2\text{F}_{7/2} \rightarrow {}^2\text{F}_{5/2}$ (Yb^{3+}) transition [37]. In Fig. 3 (b), the diffuse reflectance spectrum of $\text{Nd}^{3+}/\text{Er}^{3+}/\text{Yb}^{3+}$ tri-doped $\text{Ba}_2\text{GdV}_3\text{O}_{11}$ phosphors is presented. A prominent absorption peak is observed at 304 nm, ascribed to charge transfer band from the oxygen ligands to the center of vanadium. Furthermore, additional absorption peaks are observed at 524, 593, 657, 752, 808, and 878 nm, associated with the presence of Er^{3+} and Nd^{3+} ions [38]. In the 900–1000 nm range, an absorption feature is observed, which can be attributed to ${}^2\text{F}_{7/2} \rightarrow {}^2\text{F}_{5/2}$ (Yb^{3+}) [37].

The band gap (E_g) of $\text{Ba}_2\text{GdV}_3\text{O}_{11}$ phosphors is determined using the diffuse reflectance spectrum according to the Kubelka-Munk (KM) theory [39–43]. The KM remission function, denoted as $F(R_\infty)$, relates the diffuse reflectance (R_∞) to the absorption coefficient (k), scattering coefficient (S), and absorption coefficient of the material (α) [29]:

$$F(R_\infty) = \alpha = \frac{k}{S} = \frac{(1 - R_\infty)^2}{2R_\infty} \quad (1)$$

The Tauc equation establishes a correlation between the band gap energy (E_g) and the absorption coefficient, characterized by a parabolic band structure:

$$[F(R_\infty)hv]^n = B(hv - E_g) \quad (2)$$

In this equation, "hv" represents the photon energy, "B" stands for a constant proportionality factor, and "n" is a variable dependent on the type of optical transition occurring within the material. The value of "n" varies according to the nature of the optical transition. For instance, a value of "n = 2" corresponds to an indirect allowed transition, "n = 3" to an indirect forbidden transition, "n = 1/2" to a direct allowed transition, and "n = 3/2" to a direct forbidden transition.

In the plot of $[F(R_\infty)hv]^2$ versus hv , a direct allowed transition displays both linear and nonlinear sections. The linear segment corresponds to fundamental absorption, while the nonlinear segment represents residual absorption involving impurity states. In the present analysis, extrapolating the line for $[F(R_\infty)hv]^2 = 0$ (refer to Fig. 3(c) and (d)), it is observed that the optical band gap is 3.06 eV in the $\text{Ho}^{3+}/\text{Er}^{3+}/\text{Yb}^{3+}$ doped $\text{Ba}_2\text{GdV}_3\text{O}_{11}$ phosphor and 3.00 eV in the $\text{Nd}^{3+}/\text{Er}^{3+}/\text{Yb}^{3+}$ doped $\text{Ba}_2\text{GdV}_3\text{O}_{11}$ phosphor. Therefore, it can be inferred that the introduction of Nd^{3+} ions leads to a reduction in the energy band gap. It is worth mentioning that the energy band gap decreased from 3.60 eV [32] for Er^{3+} doped $\text{Ba}_2\text{GdV}_3\text{O}_{11}$ to 3.00 eV for the $\text{Nd}^{3+}/\text{Er}^{3+}/\text{Yb}^{3+}$ doped $\text{Ba}_2\text{GdV}_3\text{O}_{11}$ phosphor.

The room temperature UC spectrum of $\text{Ho}^{3+}/\text{Er}^{3+}/\text{Yb}^{3+}$ tri-doped $\text{Ba}_2\text{GdV}_3\text{O}_{11}$ phosphors upon 980 nm excitation is shown in Fig. 4(a). The spectrum exhibits three distinct peaks in the 500–700 nm range, corresponding to two green emissions at 525 nm and 555 nm, and red emission at ~665 nm. These peaks correspond to the ${}^2\text{H}_{11/2} \rightarrow {}^4\text{I}_{15/2}$ (Er^{3+}), ${}^5\text{S}_2/{}^5\text{F}_4 \rightarrow {}^5\text{I}_8$ (Ho^{3+}) + ${}^4\text{S}_{3/2} \rightarrow {}^4\text{I}_{15/2}$ (Er^{3+}), and ${}^5\text{F}_5 \rightarrow {}^5\text{I}_8$ (Ho^{3+}) + ${}^4\text{F}_{9/2} \rightarrow {}^4\text{I}_{15/2}$ (Er^{3+}) transitions, respectively [27,35,44]. Importantly, there exists considerable spectral overlap among the emission bands of Ho^{3+} (${}^5\text{F}_5 \rightarrow {}^5\text{I}_8$) and Er^{3+} (${}^4\text{F}_{9/2} \rightarrow {}^4\text{I}_{15/2}$) in the 635–685 nm region. Thus, the emission band within this region is likely attributed to the combined contributions of Ho^{3+} and Er^{3+} ions [27]. Fig. 4(b) illustrates the room

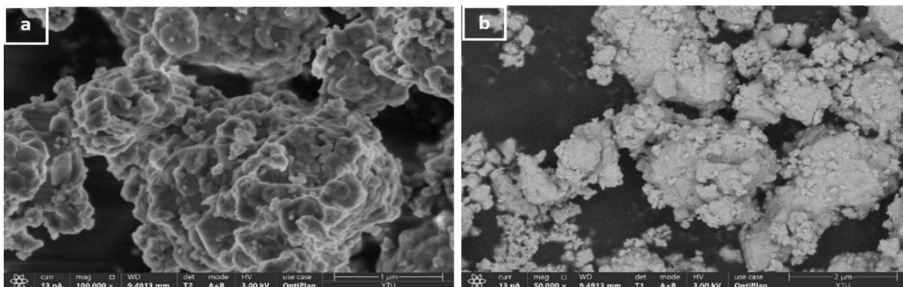


Fig. 2. FE-SEM images of (a) $\text{Ho}^{3+}/\text{Er}^{3+}/\text{Yb}^{3+}$, (b) $\text{Nd}^{3+}/\text{Er}^{3+}/\text{Yb}^{3+}$ tri-doped $\text{Ba}_2\text{GdV}_3\text{O}_{11}$ phosphors.

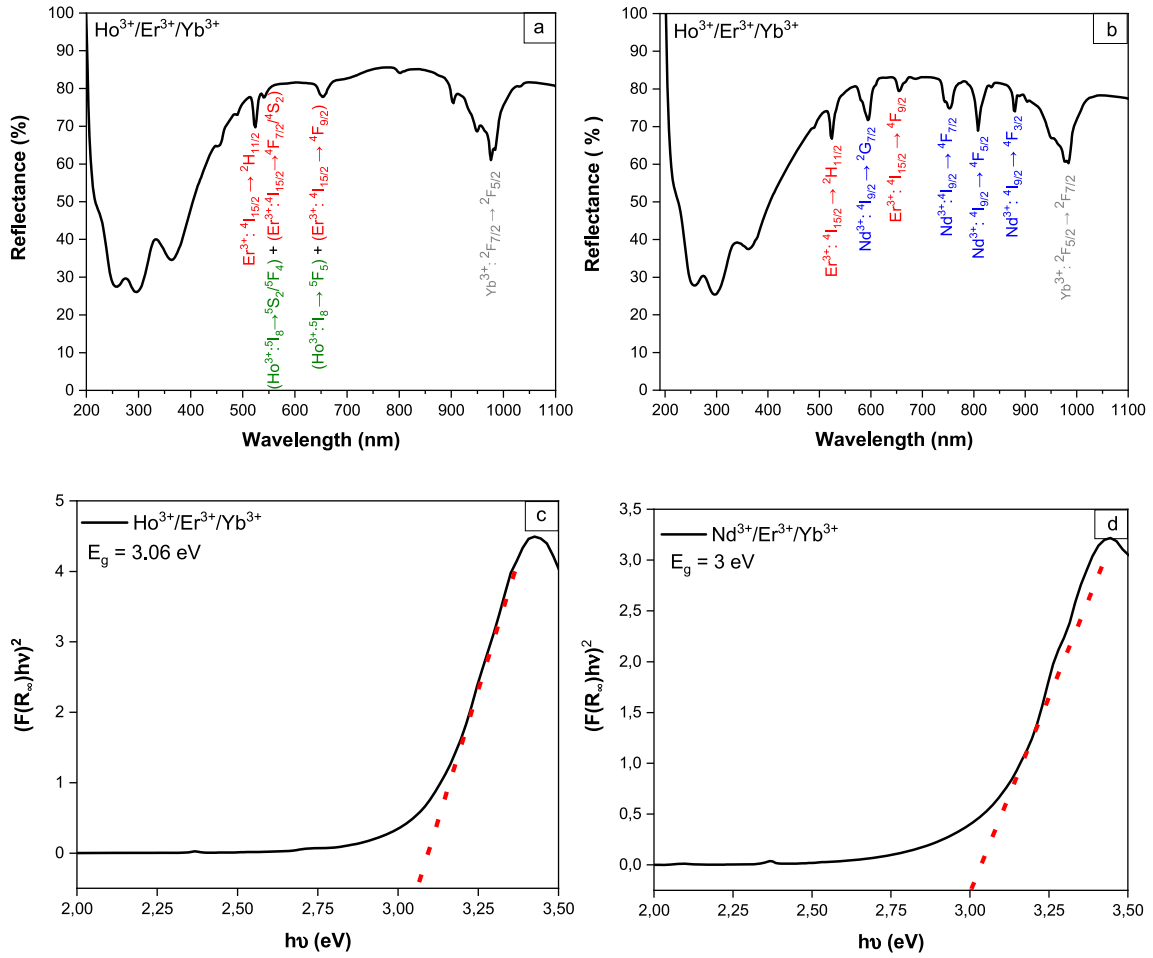


Fig. 3. (a), (b) Diffuse reflectance spectra, and (c), (d) plots of $[F(R_{\infty})hv]^2$ versus $h\nu$ of $\text{Ho}^{3+}/\text{Er}^{3+}/\text{Yb}^{3+}$ and $\text{Nd}^{3+}/\text{Er}^{3+}/\text{Yb}^{3+}$ tri-doped $\text{Ba}_2\text{GdV}_3\text{O}_{11}$ phosphors, respectively.

temperature UC emission characteristics of $\text{Nd}^{3+}/\text{Er}^{3+}/\text{Yb}^{3+}$ tri-doped $\text{Ba}_2\text{GdV}_3\text{O}_{11}$ phosphors upon 980 nm excitation. The prominent peak observed at 525 nm corresponds to the $\text{Er}^{3+} \ ^2\text{H}_{11/2} \rightarrow \ ^4\text{I}_{15/2}$ transition. Additionally, the emission bands at 582 nm arise from Nd^{3+} ions, while the 665 nm and 690 nm red emissions are ascribed to Er^{3+} and Nd^{3+} ions, respectively. Notably, there is a substantial spectral overlap among the emission bands of $\text{Er}^{3+} \ (^4\text{S}_{3/2} \rightarrow \ ^4\text{I}_{15/2})$ and $\text{Nd}^{3+} \ (^2\text{G}_{7/2} \rightarrow \ ^4\text{I}_{9/2})$ in the 530–565 nm region [45]. Thus, the emission band within this region is likely attributed to the combined contributions of Er^{3+} and Nd^{3+} ions [46]. The emission from coupled energy levels of Er^{3+} becomes more intense when Nd^{3+} ions are introduced into the $\text{Er}^{3+}/\text{Yb}^{3+}$ doped phosphor. Conversely, the inclusion of Ho^{3+} ions into the $\text{Er}^{3+}/\text{Yb}^{3+}$ doped phosphor leads to an enhancement in the emission intensity within the red region, as depicted in Fig. 4(c). The introduction of Nd^{3+} ions have been associated with an increase in the green emission intensity of Er^{3+} ions and an influence on the luminescent properties of sample, indicating the potential for Nd^{3+} doping to enhance the optical efficiency and emission characteristics of these materials. It's worth noting that, in addition to emitting light in the green and red regions, albeit with relatively low intensity, the contributions of Ho^{3+} and Nd^{3+} ions frequently manifest through intricate energy transfer processes among various ions' energy levels.

The introduction of Nd^{3+} doping in $\text{Ba}_2\text{GdV}_3\text{O}_{11}$ induces a slight reduction in the band gap, from 3.06 eV to 3 eV, when transitioning from $\text{Ho}^{3+}/\text{Er}^{3+}/\text{Yb}^{3+}$ tri-doped to $\text{Nd}^{3+}/\text{Er}^{3+}/\text{Yb}^{3+}$ tri-doped samples. However, this change doesn't directly affect the upconversion process. Upon 980 nm excitation, low-energy photons are primarily excited via Yb^{3+} sensitizer ions to Er^{3+} activator ions. The increase in upconversion emission intensity in Nd^{3+} -doped samples is attributed to more resonant energy transfer between Yb^{3+} , Nd^{3+} , and Er^{3+} ions, leading to a more efficient population of emitter levels. Additionally, Nd^{3+} introduction influences energy transfer mechanisms involved in upconversion processes, such as sensitization and cooperative processes.

In practice, color coordinates are employed to compare different phosphors. The chromaticity coordinates of $\text{Ho}^{3+}/\text{Er}^{3+}/\text{Yb}^{3+}$ and $\text{Nd}^{3+}/\text{Er}^{3+}/\text{Yb}^{3+}$ tri-doped $\text{Ba}_2\text{GdV}_3\text{O}_{11}$ phosphors are calculated to be $(x = 0.369, y = 0.616)$ and $(x = 0.299, y = 0.684)$, respectively (see Fig. 4(d)). The CIE coordinates of the phosphors exhibit suitability for applications requiring green luminescence, surpassing findings from prior studies. Color purity can be calculated using a specific equation outlined in the literature [47,48].

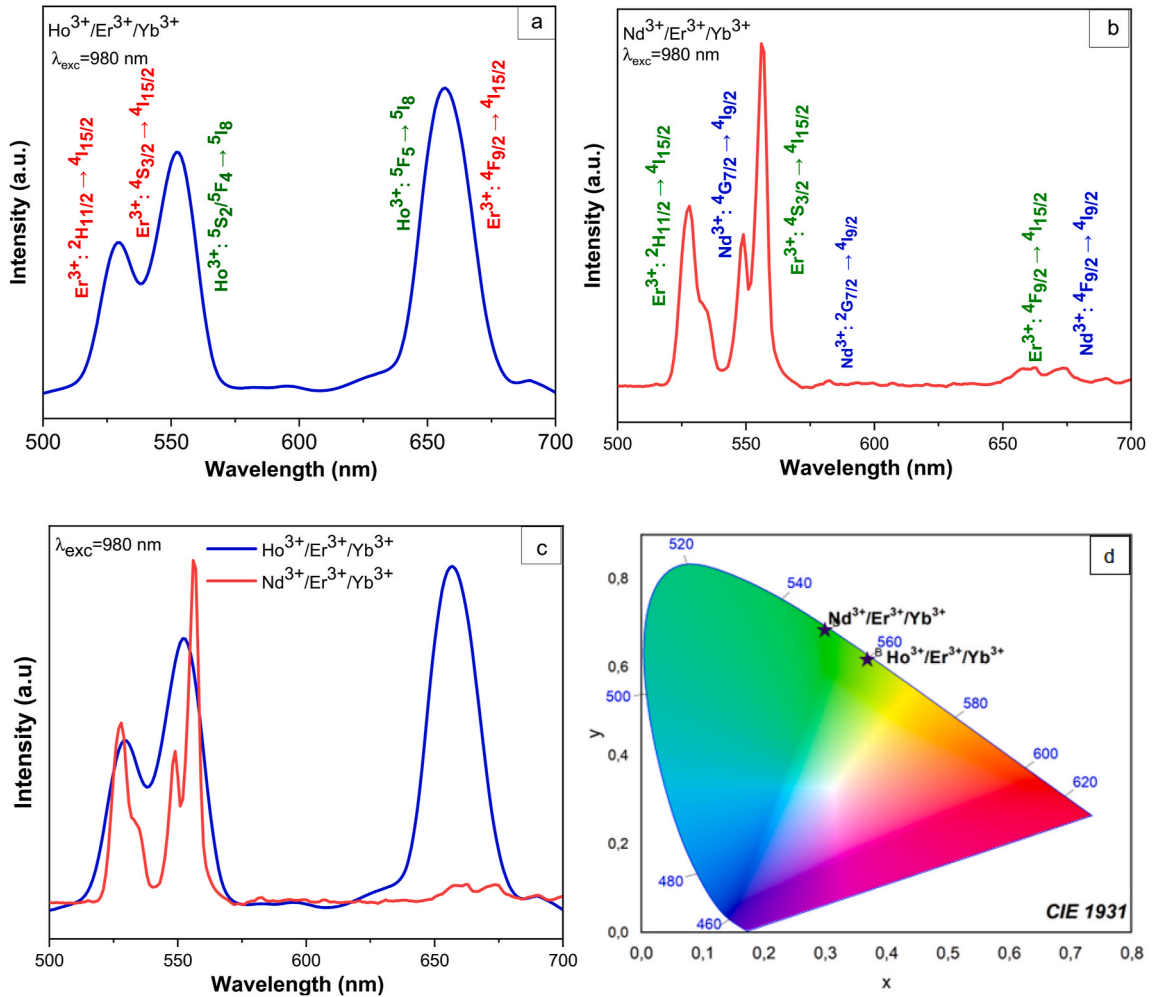


Fig. 4. Upconversion emission spectrum under 980 nm excitation for (a) $\text{Ho}^{3+}/\text{Er}^{3+}/\text{Yb}^{3+}$ and (b) $\text{Nd}^{3+}/\text{Er}^{3+}/\text{Yb}^{3+}$ doped $\text{Ba}_2\text{GdV}_3\text{O}_{11}$ phosphors (c) superposition of $\text{Ho}^{3+}/\text{Er}^{3+}/\text{Yb}^{3+}$ and $\text{Nd}^{3+}/\text{Er}^{3+}/\text{Yb}^{3+}$ emissions (d) chromaticity diagram of $\text{Ho}^{3+}/\text{Nd}^{3+}$, Er^{3+} , Yb^{3+} upon 980 nm excitation.

$$\text{Color purity} = \frac{\sqrt{((x - x_i)^2 + (y - y_i)^2)}}{\sqrt{(x_d - x_i)^2 + (y_d - y_i)^2}} \quad (3)$$

In this context, (x, y) represents the CIE coordinate of the samples, while (x_i, y_i) signifies the white illumination CIE coordinates, and (x_d, y_d) denotes the CIE coordinate of the dominated wavelength. The calculated color purity for the two phosphors reveals values of 84 % and 99 % for $\text{Ho}^{3+}/\text{Er}^{3+}/\text{Yb}^{3+}$ and $\text{Nd}^{3+}/\text{Er}^{3+}/\text{Yb}^{3+}$, respectively. Notably, the sample doped with Nd^{3+} exhibits a higher color quality, making it potentially suitable for applications in displays.

3.2. Power-dependent luminescence characteristics and UC mechanism

Exploring the power-dependent upconversion (UC) emission intensities (I) offers valuable insights into the underlying UC luminescence process. To achieve a more profound comprehension of the UC process in $\text{Ho}^{3+}/\text{Er}^{3+}/\text{Yb}^{3+}$ and $\text{Nd}^{3+}/\text{Er}^{3+}/\text{Yb}^{3+}$ tri-doped $\text{Ba}_2\text{GdV}_3\text{O}_{11}$ phosphors, the investigation focuses on the relationship between the integrated intensity of the UC emission and the laser pump power (P). This relationship is described by the following equation [49]:

$$I = K \times P^n \quad (4)$$

In the provided equation, "K" stands as a constant, and "n" denotes the count of infrared photons essential for the population of a particular excitation level. Analysis of log intensity versus log laser power density plots unveils a clear linear correlation with the experimental data. In this context, excitation power density is described as the quantity of power reaching the surface of the phosphor

divided by the exposed area.

By analyzing the slopes of the emission intensity versus excitation power density curves, the value of n can be estimated more explicitly (see in Fig. 5(a) and (b)). To determine the number of infrared photons involved, the emission peaks at 555 nm and 665 nm are specifically chosen due to their significant intensity and sensitivity to laser pump power density. The slopes for the 555 nm and 665 nm emission peaks in the $\text{Ho}^{3+}/\text{Er}^{3+}/\text{Yb}^{3+}$ tri-doped $\text{Ba}_2\text{GdV}_3\text{O}_{11}$ phosphors under 980 nm excitation are determined to be 1.8 and 1.96, respectively. While the calculated values of n for the 555 nm and 665 nm emission peaks in the $\text{Nd}^{3+}/\text{Er}^{3+}/\text{Yb}^{3+}$ tri-doped $\text{Ba}_2\text{GdV}_3\text{O}_{11}$ phosphors under 980 nm excitation are 2.02 and 1.89, respectively. These results indicate that the UC processes involved in the $\text{Ho}^{3+}/\text{Er}^{3+}/\text{Yb}^{3+}$ and $\text{Nd}^{3+}/\text{Er}^{3+}/\text{Yb}^{3+}$ and tri-doped $\text{Ba}_2\text{GdV}_3\text{O}_{11}$ phosphors are two-photon processes [46,50].

Utilizing the established connection between upconversion (UC) emission intensity and pump power, Figs. 6 and 7 present schematic representations of the energy level structure and potential energy transfer (ET) processes between Ho^{3+} , Er^{3+} , Yb^{3+} ions, and Nd^{3+} , Er^{3+} , Yb^{3+} ions under 980 nm excitation. These illustrations offer additional insights into the UC luminescence mechanism. As illustrated in Fig. 6, in the energy transfer process involving Ho^{3+} , Er^{3+} , and Yb^{3+} ions, the initial step involves the excitation of the $^2\text{F}_{7/2}$ level of Yb^{3+} to the $^2\text{F}_{5/2}$ level through ground state absorption (GSA) upon being pumped with a 980 nm laser. Subsequently, the energy can be transferred to the $^5\text{I}_6$ level of Ho^{3+} and the $^4\text{I}_{11/2}$ level of Er^{3+} . GSA can also occur for the $^4\text{I}_{15/2} \rightarrow ^4\text{I}_{11/2}$ transition in Er^{3+} under 980 nm excitation. Remarkably, Yb^{3+} ions demonstrate a greater absorption cross-section at 980 nm in comparison to Ho^{3+} and Er^{3+} ions, facilitating efficient energy transfer due to the spectral overlap between the $^2\text{F}_{5/2}$ and $^2\text{F}_{7/2}$ emission of Yb^{3+} and the $^4\text{I}_{15/2}$ absorption bands of Er^{3+} (ET₁).

As a result of ET₁, the population of the Er^{3+} ion in the $^4\text{I}_{11/2}$ state is enhanced, allowing for a transition from the $^4\text{I}_{11/2}$ state to the $^4\text{F}_{7/2}$ state and subsequently to the $^4\text{G}_{11/2}$ state. Non-radiative relaxations can then populate the $^2\text{H}_{11/2}$ and $^4\text{S}_{3/2}$ states, corresponding to the emission levels of green luminescence. Alternatively, the $^4\text{I}_{11/2}$ states of Er^{3+} ions may undergo relaxation to the $^4\text{I}_{13/2}$ state, leading to red emission in the $^4\text{F}_{9/2}$ levels.

Similarly, the Ho^{3+} ion undergoes energy transfer (ET₂) to populate the $^5\text{I}_6$ state, allowing for transitions from the $^5\text{I}_6$ state to the $^5\text{F}_4$ state, resulting in the emission of green luminescence. If the $^5\text{I}_6$ state of the Ho^{3+} ion relaxes non-radiatively to the $^5\text{I}_7$ state, it can be excited to the $^5\text{F}_5$ state, resulting in red emission [51].

Phosphors under 980 nm excitation.

Fig. 7 illustrates the energy level diagrams of Nd^{3+} , Er^{3+} , Yb^{3+} ions and the proposed UC emission mechanisms under 980 nm excitation. Initially, the excitation of Yb^{3+} ions from the ground state $^2\text{F}_{7/2}$ to the excited state $^2\text{F}_{5/2}$ occurs through GSA. The ground state of Er^{3+} ions is stimulated to the $^4\text{I}_{11/2}$ state. Subsequently, the Er^{3+} ions at the $^4\text{I}_{11/2}$ state can populate the $^4\text{F}_{7/2}$ state through non-radiative relaxation. From the $^4\text{F}_{7/2}$ state, further non-radiative relaxation leads to the population of the $^2\text{H}_{11/2}$ and $^4\text{S}_{3/2}$ levels. The Er^{3+} ions at these levels then relax to the $^4\text{I}_{15/2}$ state, resulting in the green emission at 525 nm and 555 nm, respectively. The multi-phonon relaxation mechanism allows the relaxation of the Er^{3+} ions from the $^4\text{I}_{11/2}$ state to the $^4\text{I}_{13/2}$ state before being stimulated to the $^4\text{F}_{9/2}$ state. Non-radiative relaxation also enables the population of the $^4\text{F}_{9/2}$ state from the $^4\text{S}_{3/2}$ state. The transition of Er^{3+} ions from the $^4\text{F}_{9/2}$ state to the $^4\text{I}_{15/2}$ state emits red light at 665 nm. Regarding Nd^{3+} ions, they are stimulated from the $^4\text{I}_{9/2}$ state to the $^4\text{F}_{3/2}$ state. Cooperative excitation assists in populating the $^2\text{G}_{9/2}$ state of Nd^{3+} ions. In this process, the Nd^{3+} ions are excited from the $^4\text{I}_{9/2}$ state to the $^2\text{G}_{9/2}$ state, followed by non-radiative relaxation to the $^4\text{G}_{7/2}$ and $^2\text{G}_{7/2}$ states. Ultimately, relaxation from the $^4\text{G}_{7/2}$ and $^2\text{G}_{7/2}$ states to the $^4\text{I}_{9/2}$ state leads to low-intensity green emission at 550 nm and low-intensity yellow emission at 582 nm, respectively [46].

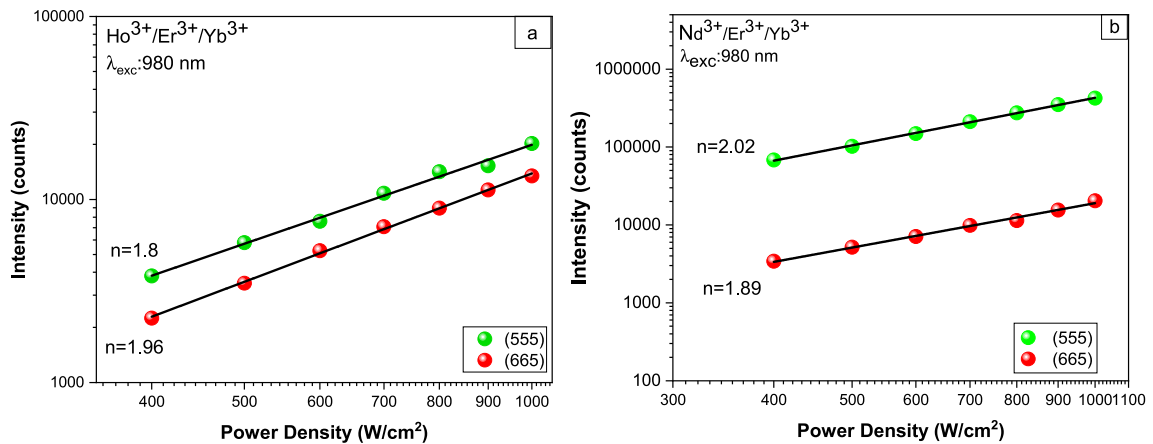


Fig. 5. The integral emission intensity of the green (555 nm) and red (665 nm) emission bands is examined as a function of the pump laser power under 980 nm excitation for (a) $\text{Ho}^{3+}/\text{Er}^{3+}/\text{Yb}^{3+}$ and (b) $\text{Nd}^{3+}/\text{Er}^{3+}/\text{Yb}^{3+}$ tri-doped $\text{Ba}_2\text{GdV}_3\text{O}_{11}$ phosphors. (For interpretation of the references to color in this figure legend, the reader is referred to the Web version of this article.)

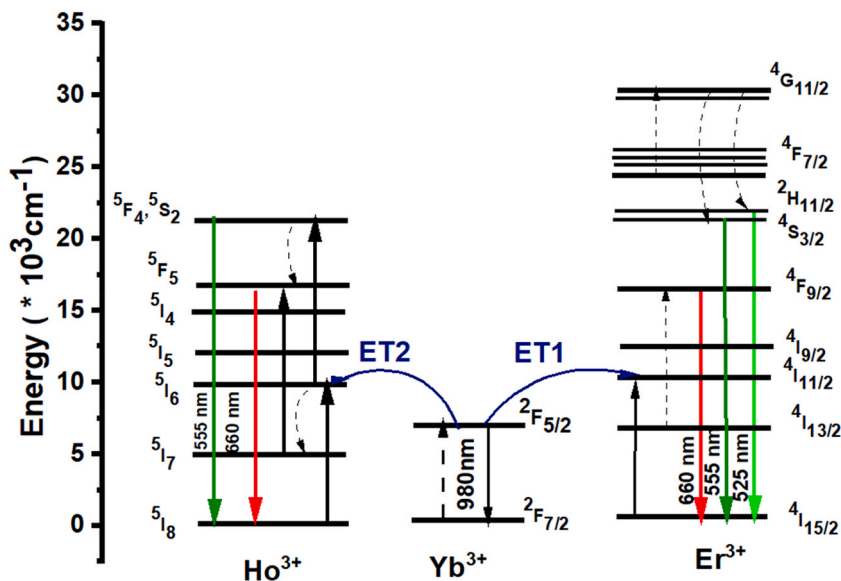


Fig. 6. Energy transfer pathways in $\text{Ho}^{3+}/\text{Er}^{3+}/\text{Yb}^{3+}$ tri-doped $\text{Ba}_2\text{GdV}_3\text{O}_{11}$ phosphors under 980 nm excitation.

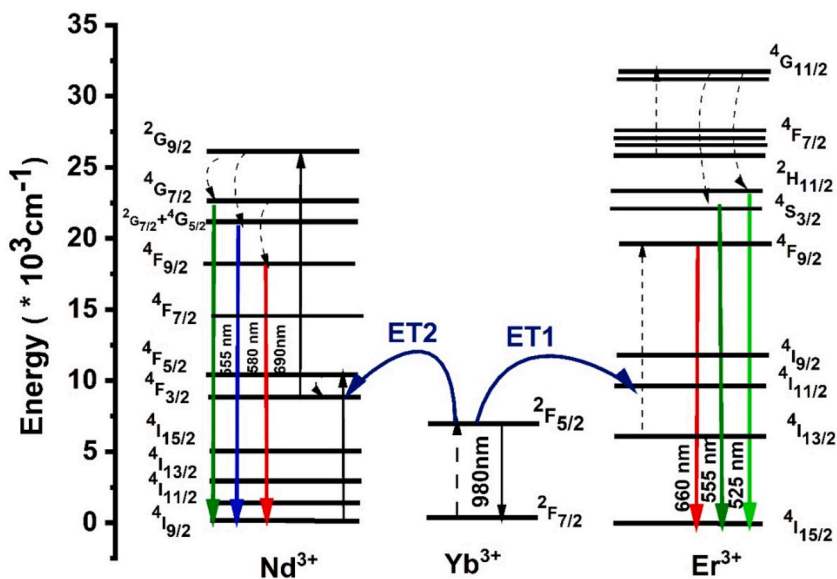


Fig. 7. Energy transfer pathways in $\text{Nd}^{3+}/\text{Er}^{3+}/\text{Yb}^{3+}$ tri-doped $\text{Ba}_2\text{GdV}_3\text{O}_{11}$.

3.3. Temperature-responsive UC emission and optical temperature-sensing characteristics

The temperature-dependent UC emission spectra excited by a 980 nm laser are presented in Fig. 8(a) and (b) to evaluate the potential of $\text{Ho}^{3+}/\text{Er}^{3+}/\text{Yb}^{3+}$ and $\text{Nd}^{3+}/\text{Er}^{3+}/\text{Yb}^{3+}$ tri-doped $\text{Ba}_2\text{GdV}_3\text{O}_{11}$ phosphors as temperature sensors. To prevent the heating due to excitation, we have maintained the excitation power level at 0.5 W [52,53]. This ensures that the temperature increase resulting from the excitation is minimized and allows for accurate assessment of the temperature-dependent luminescence properties [54]. Firstly, as shown in Fig. 8(a) two different green emissions peaks are investigated to illustrate the variation tendency of the intensity ratio as the temperature rises from 298 to 573 K. The UCL intensities of the ${}^2\text{H}_{11/2} \rightarrow {}^4\text{I}_{15/2}$ (Er^{3+}) transition at 525 nm exhibits an increase, while the UCL intensities of the ${}^5\text{S}_2/{}^5\text{F}_4 \rightarrow {}^5\text{I}_8$ (Ho^{3+}) + ${}^4\text{S}_{3/2} \rightarrow {}^4\text{I}_{15/2}$ (Er^{3+}) transitions at 555 nm shows a noticeable decrease in intensity as temperature increases. Additionally, the red UCL intensities of the ${}^5\text{F}_5 \rightarrow {}^5\text{I}_8$ (Ho^{3+}) + ${}^4\text{F}_{9/2} \rightarrow {}^4\text{I}_{15/2}$ (Er^{3+}) transitions at ~ 665 nm gradually decreases. The UC emission spectra of $\text{Nd}^{3+}/\text{Er}^{3+}/\text{Yb}^{3+}$ tri-doped $\text{Ba}_2\text{GdV}_3\text{O}_{11}$ phosphors under 980 nm excitation at various temperatures are shown in Fig. 8(b). With rising temperature, there is an increase in the intensity of the ${}^2\text{H}_{11/2} \rightarrow {}^4\text{I}_{15/2}$ transition (Er^{3+}) at 525 nm in UCL. Conversely, the UCL intensities of the ${}^4\text{S}_{3/2} \rightarrow {}^4\text{I}_{15/2}$ (Er^{3+}) + (${}^4\text{G}_{7/2} \rightarrow {}^4\text{I}_{9/2}$) (Nd^{3+}) at

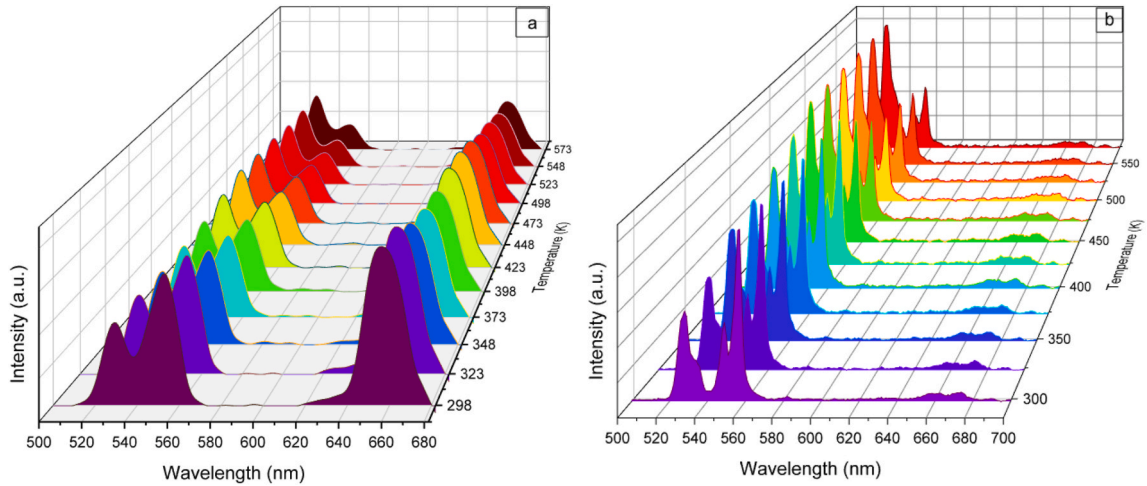


Fig. 8. Temperature-dependent UC emission spectra (a) of $\text{Ho}^{3+}/\text{Er}^{3+}/\text{Yb}^{3+}$ and (b) $\text{Nd}^{3+}/\text{Er}^{3+}/\text{Yb}^{3+}$ tri-doped $\text{Ba}_2\text{GdV}_3\text{O}_{11}$ phosphors under 980 nm excitation respectively.

530–565 nm demonstrate a decrease with increasing temperature.

To evaluate the influence of temperature fluctuations on the intensity of the distinct peaks at 525 nm and 555 nm, it is essential to compute the ratio of intensities between the two peaks. This ratio consistently rises with temperature. The Boltzmann distribution governs the population ratio of the two transitions (525 nm and 555 nm) relative to temperature, and the fluorescence intensity ratio (FIR) can be described using the following equation [55]:

$$FIR = \frac{I_2}{I_1} = B \exp\left(\frac{-\Delta E}{K_B T}\right) \quad (5)$$

where I_2 and I_1 represent the integrated intensities of two different transitions, ΔE denotes the energy difference between these two levels, K_B is the Boltzmann constant with a value of $0.695 \text{ cm}^{-1}\text{K}^{-1}$, A is a constant determined by the degeneracy, spontaneous emission rate, and photon energies of the emitting states in the host material, and B is a parameter associated with the curve of the FIR plotted against the $1/T$ [56]. For $\text{Ho}^{3+}/\text{Er}^{3+}/\text{Yb}^{3+}$ and $\text{Nd}^{3+}/\text{Er}^{3+}/\text{Yb}^{3+}$ tri doped $\text{Ba}_2\text{GdV}_3\text{O}_{11}$ phosphors, the FIR values present an increasing tendency with temperature, as displayed in Fig. 9(a) and (b). FIR as a function of temperature can be fitted by Eq. (5) with a regression coefficient (R^2) of 0.99 based on the previous results. According to the results of the fit, the ΔE values is 639.4 cm^{-1} for $\text{Ho}^{3+}/\text{Er}^{3+}/\text{Yb}^{3+}$ doped phosphors and 656.71 cm^{-1} for $\text{Nd}^{3+}/\text{Er}^{3+}/\text{Yb}^{3+}$ doped phosphors. Thus, the slight fluctuations observed during the calculation of the ΔE values might be ascribed to a multifaceted dynamic process governing the population between the $^2\text{H}_{11/2}$ and $^4\text{S}_{3/2}$ levels, which are affected by Ho^{3+} and Nd^{3+} dopants neighboring Er^{3+} ions.

To get deeper understanding on the optical temperature sensing behavior it is essential to determining the absolute sensitivity (S_a) and relative sensitivity (S_r) [57]. The following equations can be utilized to compute the sensitivities [58]:

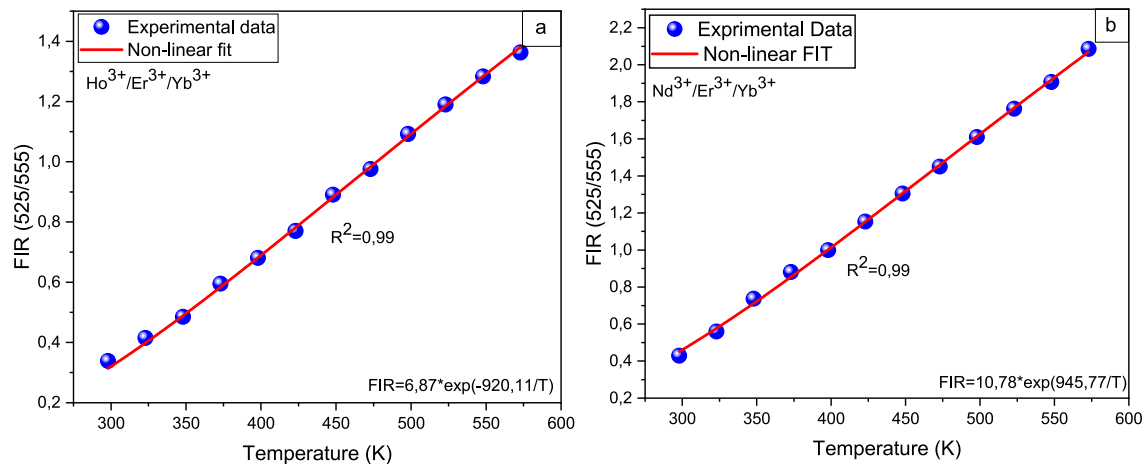


Fig. 9. FIR vs temperature variations for the green emission (a) of $\text{Ho}^{3+}/\text{Er}^{3+}/\text{Yb}^{3+}$ and (b) $\text{Nd}^{3+}/\text{Er}^{3+}/\text{Yb}^{3+}$ tri-doped $\text{Ba}_2\text{GdV}_3\text{O}_{11}$ phosphors. (For interpretation of the references to color in this figure legend, the reader is referred to the Web version of this article.)

$$S_a = \frac{dFIR}{dT} \quad (6)$$

$$S_r = \frac{1}{FIR} \frac{\delta FIR}{\delta T} \quad (7)$$

Fig. 10(a) and (b) illustrate the calculated S_a parameter for two distinct phosphors. The data clearly indicate that, with the rise in temperature, the absolute sensitivity of the sensor increases, reaching its peak at 450 K. For the $\text{Ho}^{3+}/\text{Er}^{3+}/\text{Yb}^{3+}$ phosphor, S_a attains a maximum value of 0.0041 K^{-1} , while for the $\text{Nd}^{3+}/\text{Er}^{3+}/\text{Yb}^{3+}$ phosphor, the maximum is reached at 473 K with S_a equal to 0.0061 K^{-1} . It is noteworthy that the S_a value holds greater significance for the $\text{Nd}^{3+}/\text{Er}^{3+}/\text{Yb}^{3+}$ doped $\text{Ba}_2\text{GdV}_3\text{O}_{11}$ phosphor. Meanwhile, the S_r parameter experiences a decrease with increasing temperature, reaching maximum values of $1.03 \% \text{ K}^{-1}$ and $1.07 \% \text{ K}^{-1}$ for $\text{Ho}^{3+}/\text{Er}^{3+}/\text{Yb}^{3+}$ and $\text{Nd}^{3+}/\text{Er}^{3+}/\text{Yb}^{3+}$ doped $\text{Ba}_2\text{GdV}_3\text{O}_{11}$ phosphors, respectively (refer to Fig. 10(a) and (b)). Crucially, we compare these sensitivities to similar studies outlined in Table 1, highlighting that the sensitivities determined in this study surpass those reported for many other phosphors. Given these results, it can be inferred that the $\text{Ho}^{3+}/\text{Er}^{3+}/\text{Yb}^{3+}$ and $\text{Nd}^{3+}/\text{Er}^{3+}/\text{Yb}^{3+}$ tri-doped $\text{Ba}_2\text{GdV}_3\text{O}_{11}$ phosphor exhibits promising potential as a temperature-sensing material.

The temperature uncertainty (δT), which serves as an important indicator of the thermometer's effectiveness, denotes the minimum temperature alteration that induces a noteworthy change in the measured parameter. The estimation of δT is obtained using the following equation [65]:

$$\delta T = \frac{\delta FIR}{FIR} \times \frac{1}{S_r} \quad (8)$$

In the given formula, δFIR symbolizes the resolution threshold or the relative uncertainty associated with the thermometric parameter. This value denotes the minimum discernible alteration in the ratio that can be identified through empirical observation. It's crucial to emphasize that the resolution limit isn't solely determined by the efficacy of the thermometer but is also impacted by the attributes of the experimental arrangement [66]. Consequently, one approach to enhancing the resolution limit involves the implementation of advanced acquisition techniques. This encompasses measures such as improving integration time and employing the averaging of successive measurements to diminish experimental noise. To assess the limit of detection, a series of 40 measurements is conducted at room temperature under conditions comparable to those employed for $\text{Ho}^{3+}/\text{Nd}^{3+}$, Er^{3+} , Yb^{3+} tri-doped $\text{Ba}_2\text{GdV}_3\text{O}_{11}$ phosphors.

The standard deviations for FIR ($\text{Ho}^{3+}/\text{Er}^{3+}/\text{Yb}^{3+}$) and FIR ($\text{Nd}^{3+}/\text{Er}^{3+}/\text{Yb}^{3+}$) tri-doped $\text{Ba}_2\text{GdV}_3\text{O}_{11}$ phosphors obtained using 40 measurements at 298 K, are represented in Fig. 11(a) and (b) respectively. Temperature uncertainties (δT) for different FIR are calculated as a function of temperature and are shown in Fig. 12(a) and (b). Applying the FIR strategy, the δT values ranged from 0.084 K to 0.067 K for $\text{Ho}^{3+}/\text{Er}^{3+}/\text{Yb}^{3+}$ doped $\text{Ba}_2\text{GdV}_3\text{O}_{11}$ phosphor and from 0.042 K to 0.033 K for $\text{Nd}^{3+}/\text{Er}^{3+}/\text{Yb}^{3+}$ doped $\text{Ba}_2\text{GdV}_3\text{O}_{11}$, respectively. Significantly, each computed δT value is consistently below 0.1 K, underscoring the remarkable accuracy of both phosphors across the entire temperature range. This emphasizes the significance of these phosphors in optical thermometry.

3.4. Temperature dependent lifetime analysis

Aside from the techniques involving FIR, the FL technique holds significant importance in optical thermometry. Therefore, in this part, we focus on the transition located at 555 nm dependent on temperature fluorescence lifetimes after pulsed laser excitation (980 nm). As seen in Fig. 13(a) and (b), increasing temperature induces a substantial decrease in the Er^{3+} UC lifetime, which is most likely owing to the amplification of nonradiative transitions. Fig. 13(c) and (d) represent the decay time variations with temperature. The average lifetime of Er^{3+} ions in the ${}^4\text{S}_{3/2}$ state experiences a decline from $23.415 \mu\text{s}$ to $17.209 \mu\text{s}$ for $\text{Ho}^{3+}/\text{Er}^{3+}/\text{Yb}^{3+}$ tri-doped $\text{Ba}_2\text{GdV}_3\text{O}_{11}$ phosphors and from $7.611 \mu\text{s}$ to $3.342 \mu\text{s}$ for $\text{Nd}^{3+}/\text{Er}^{3+}/\text{Yb}^{3+}$ tri-doped $\text{Ba}_2\text{GdV}_3\text{O}_{11}$ phosphors with an increase in temperature from 298 to 573 K. However, as illustrated in Fig. 13(c) and (d), it becomes apparent that the lifetime decreases with

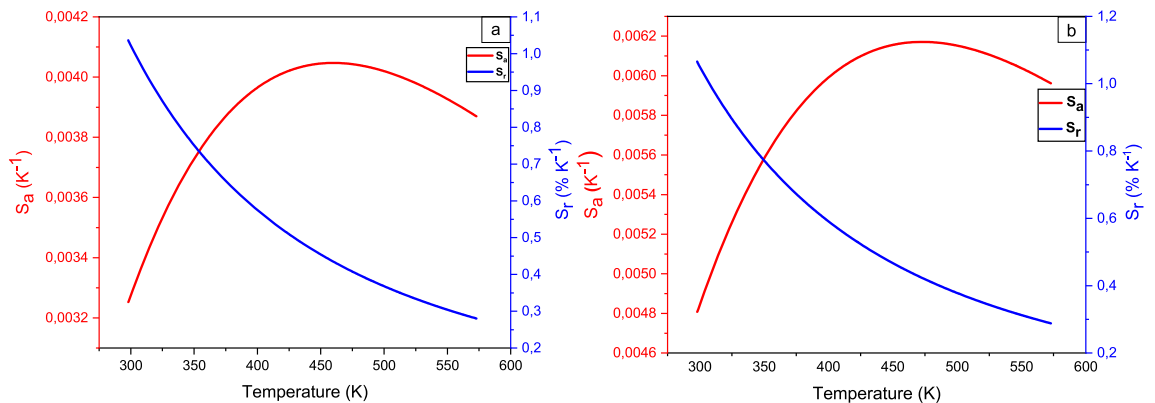


Fig. 10. The relative and absolute sensitivity of (a) of $\text{Ho}^{3+}/\text{Er}^{3+}/\text{Yb}^{3+}$ and (b) $\text{Nd}^{3+}/\text{Er}^{3+}/\text{Yb}^{3+}$ tri-doped $\text{Ba}_2\text{GdV}_3\text{O}_{11}$ phosphors.

Table 1

Comparison of the maximum S_r and S_a Parameters in $\text{Ho}^{3+}/\text{Er}^{3+}/\text{Yb}^{3+}$ and $\text{Nd}^{3+}/\text{Er}^{3+}/\text{Yb}^{3+}$ tri-doped $\text{Ba}_2\text{GdV}_3\text{O}_{11}$ phosphors using the FIR strategy against various hosts.

Host	$S_{r\max}$ (% K^{-1})	$S_{a\max}$ (K^{-1})	Temperature (K)	λ_1/λ_2 (nm)	Reference
$\text{NaLuF}_4: \text{Yb}^{3+}/\text{Er}^{3+}/\text{Ho}^{3+}$	0.74 (298 K)	–	298–503	525/547	[59]
	0.34 (503 K)	–		659/547	
$\text{CaLa}_2\text{ZnO}_5: \text{Er}^{3+}/\text{Yb}^{3+}$	–	0.0059 (513 K)	298–513	525/547	[60]
$\text{Ca}_3\text{La}_6\text{Si}_6\text{O}_{24}: \text{Yb}^{3+}/\text{Er}^{3+}/\text{Ho}^{3+}$	1.04 (293 K)	0.0039 (500 K)	298–573	525/547	[61]
Tellurite glass: $\text{Yb}^{3+}/\text{Er}^{3+}$	0.53 (298 K)	0.0089 (298 K)	298–473	525/548	[62]
$\text{LiZnPO}_4: \text{Yb}^{3+}/\text{Er}^{3+}/\text{Ho}^{3+}$	1.29 (300 K)	0.008 (440 K)	300–440	525/550	[63]
$\text{Na}_3\text{Gd}(\text{VO}_4)_2: \text{Er}^{3+}/\text{Yb}^{3+}$	0.83 (300 K)	0.0004	300–600	659/525	[27]
$\text{BaMoO}_4: \text{Yb}^{3+}/\text{Er}^{3+}$	0.47 (298 K)	–	293–573	659/525	[64]
$\text{YPVO}: \text{Er}^{3+}/\text{Yb}^{3+}/\text{Ho}^{3+}$	0.84 (298 K)	0.0032 (375 K)	298–488	525/550	[44]
$\text{Ba}_2\text{GdV}_3\text{O}_{11}: \text{Ho}^{3+}/\text{Er}^{3+}/\text{Yb}^{3+}$	1.03 (298 K)	0.0041 (475 K)	298–573	525/555	This work
$\text{Ba}_2\text{GdV}_3\text{O}_{11}: \text{Nd}^{3+}/\text{Er}^{3+}/\text{Yb}^{3+}$	1.07 (298 K)	0.0061 (475 K)			

λ_1/λ_2 (nm) corresponds to the FIR = $I_{\lambda_1}/I_{\lambda_2}$.

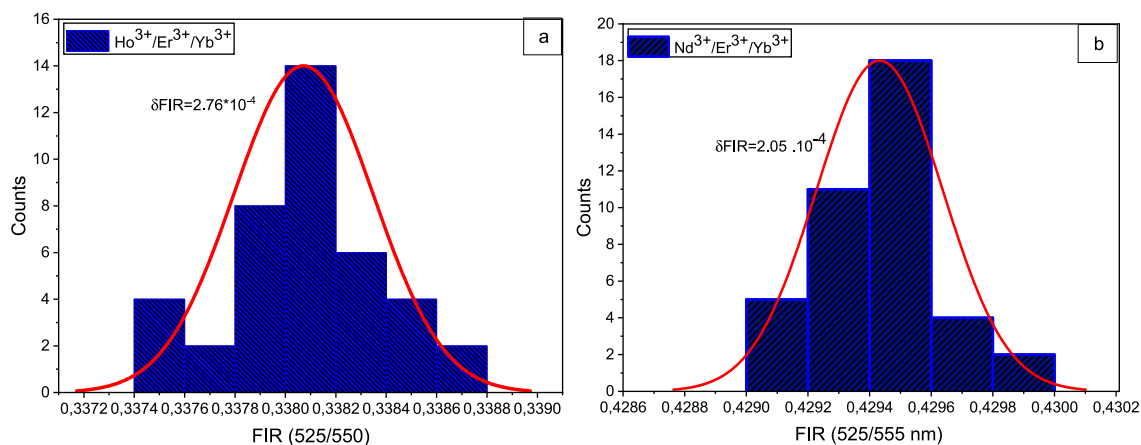


Fig. 11. Standard deviations for (a) FIR ($\text{Ho}^{3+}/\text{Er}^{3+}/\text{Yb}^{3+}$) and (b) FIR ($\text{Nd}^{3+}/\text{Er}^{3+}/\text{Yb}^{3+}$) tri-doped $\text{Ba}_2\text{GdV}_3\text{O}_{11}$ phosphors obtained using 40 measurements at 298 K.

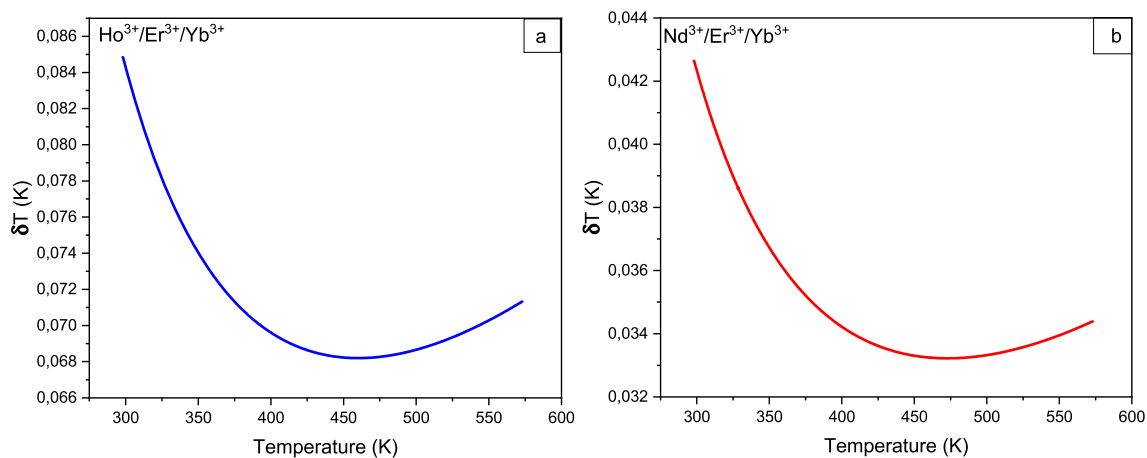


Fig. 12. Temperature resolution values δT for (a) FIR ($\text{Er}^{3+}/\text{Yb}^{3+}/\text{Ho}^{3+}$) and (b) FIR ($\text{Er}^{3+}/\text{Yb}^{3+}/\text{Nd}^{3+}$) tri-doped $\text{Ba}_2\text{GdV}_3\text{O}_{11}$ phosphors.

increasing temperature. This decline can be predominantly attributed to phonon-assisted energy transfer and multiphonon decay processes. The considerably longer decay time observed in the $\text{Ho}^{3+}/\text{Er}^{3+}/\text{Yb}^{3+}$ tri-doped $\text{Ba}_2\text{GdV}_3\text{O}_{11}$ phosphors implies more efficient energy transfer mechanisms and reduced non-radiative processes compared to the $\text{Nd}^{3+}/\text{Er}^{3+}/\text{Yb}^{3+}$ tri-doped $\text{Ba}_2\text{GdV}_3\text{O}_{11}$ phosphors. Additionally, the varying local environments surrounding the dopant ions in each sample may contribute to the observed differences in fluorescence lifetime. The fluorescence lifetime of $\text{Ho}^{3+}/\text{Er}^{3+}/\text{Yb}^{3+}$ and $\text{Nd}^{3+}/\text{Er}^{3+}/\text{Yb}^{3+}$ tri-doped $\text{Ba}_2\text{GdV}_3\text{O}_{11}$

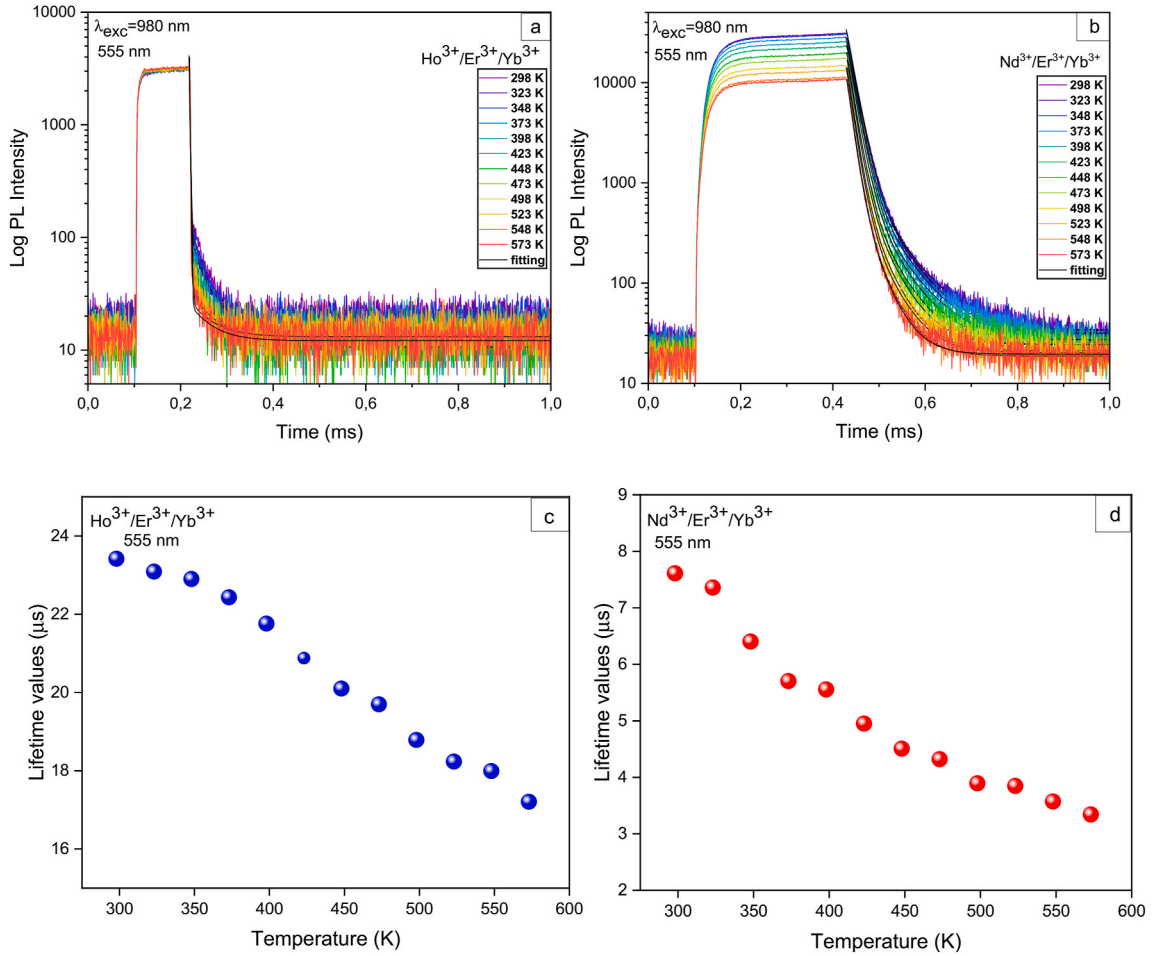


Fig. 13. (a), (b) Decay curves, and (c), (d) histogram of the decay time variations of 555 and 555 nm (⁴S_{3/2} level) emissions of Ho³⁺/Er³⁺/Yb³⁺ and Nd³⁺/Er³⁺/Yb³⁺ tri-doped Ba₂GdV₃O₁₁ phosphors at different temperatures (λ_{exc} = 980 nm), respectively.

phosphors demonstrates remarkable sensitivity to changes in temperature. Specifically, the average lifetime of Er³⁺ ions in the ⁴S_{3/2} state is calculated using the following equation [67]:

$$\tau = \frac{\int tI(t)dt}{\int I(t)dt} \tag{9}$$

In this scenario, where, where t is time, I(t) signifies the intensity of the emission, and, and τ is the average lifetime, the variation of the average decay time with temperature can be accurately described by the following equation [68,69]:

$$\frac{1}{\tau} = \frac{1}{\tau_0} \times \left[1 + Ce^{\left(\frac{-\Delta E}{kT}\right)} \right] \tag{10}$$

where τ(T) and τ₀ represent the FL at various temperatures and at 0 K, respectively. C is a constant and ΔE signifies the energy gap between ⁴F_{7/2} and ⁴S_{3/2} states.

Absolute (S_a) and relative sensitivity (S_r) values of an optical temperature sensor are determined using FL method according to the following equations:

$$S_a = \left| \frac{d\tau}{dT} \right| \tag{11}$$

$$S_r = \left| \frac{1}{\tau} \frac{\delta\tau}{\delta T} \right| \tag{12}$$

$$\delta T = \frac{\delta \tau}{\tau} \times \frac{1}{S_r} \quad (13)$$

Here, $\frac{\delta \tau}{\tau}$ is the thermometric relative parameter uncertainty. This signifies the smallest perceptible change in ratio that can be distinguished through experimental observation. It's crucial to emphasize that the resolution limit isn't solely determined by the performance of the thermometer but is also influenced by the attributes of the experimental setup [70].

The temperature dependency of the $^4S_{3/2}$ level emission average lifetime, under 980 nm excitation, for $\text{Ho}^{3+}/\text{Er}^{3+}/\text{Yb}^{3+}$ and $\text{Nd}^{3+}/\text{Er}^{3+}/\text{Yb}^{3+}$ tri-doped $\text{Ba}_2\text{GdV}_3\text{O}_{11}$ phosphors, are depicted in Fig. 14(a) and (b) respectively.

S_a and S_r values are derived and illustrated in Fig. 14(c) and (d) based on the $^4S_{3/2}$ energy levels of Er^{3+} in the context of FL temperature measurement schemes for $\text{Ho}^{3+}/\text{Er}^{3+}/\text{Yb}^{3+}$ and $\text{Nd}^{3+}/\text{Er}^{3+}/\text{Yb}^{3+}$ tri-doped $\text{Ba}_2\text{GdV}_3\text{O}_{11}$ phosphors.

The maximum values of S_r , calculated from PL of $^4S_{3/2}$ level of Er^{3+} average lifetime under 980 nm excitation are 0.146 %K⁻¹ (at 573 K) and 0.47 %K⁻¹ (at 298 K), while the highest values of S_a are 0.025 μsK⁻¹ (at 573 K) and 0.036 μsK⁻¹ (at 298 K) for $\text{Ho}^{3+}/\text{Er}^{3+}/\text{Yb}^{3+}$ and $\text{Nd}^{3+}/\text{Er}^{3+}/\text{Yb}^{3+}$ tri-doped $\text{Ba}_2\text{GdV}_3\text{O}_{11}$ phosphors, respectively. Fig. 14(e) and (f) depict the temperature uncertainty variations with temperature for $\text{Ho}^{3+}/\text{Er}^{3+}/\text{Yb}^{3+}$ and $\text{Nd}^{3+}/\text{Er}^{3+}/\text{Yb}^{3+}$ tri-doped $\text{Ba}_2\text{GdV}_3\text{O}_{11}$ phosphors, respectively.

The minimum temperature uncertainties are calculated to be 0.2 K (at 573 K) and 0.06 K (at 298 K) for $\text{Ho}^{3+}/\text{Er}^{3+}/\text{Yb}^{3+}$ and $\text{Nd}^{3+}/\text{Er}^{3+}/\text{Yb}^{3+}$ tri-doped $\text{Ba}_2\text{GdV}_3\text{O}_{11}$ phosphors, respectively.

To underscore the importance of these phosphors in thermometry applications utilizing fluorescence lifetime strategies, the sensitivities are detailed in Table 2 through the lifetime thermometry method. Notably, the S_r parameters measured in this study surpass many others reported in the literature. These results support the deduction that the $\text{Ba}_2\text{GdV}_3\text{O}_{11}$ phosphor, enriched with $\text{Ho}^{3+}/\text{Er}^{3+}/\text{Yb}^{3+}$, $\text{Nd}^{3+}/\text{Er}^{3+}/\text{Yb}^{3+}$ dopants, holds considerable promise as a temperature-sensing material.

Based on the preceding discussion, it can be inferred that $\text{Ho}^{3+}/\text{Er}^{3+}/\text{Yb}^{3+}$ and $\text{Nd}^{3+}/\text{Er}^{3+}/\text{Yb}^{3+}$ tri-doped $\text{Ba}_2\text{GdV}_3\text{O}_{11}$ phosphors demonstrate favorable upconversion (UC) emission properties and provide reliable multi-mode temperature sensitivity, as evidenced by the fluorescence intensity ratio (FIR) and fluorescence lifetime (FL) outcomes. By integrating these two optical thermometry methods simultaneously, a self-calibrating approach to temperature assessment can be attained, thereby improving the accuracy of temperature measurements.

4. Conclusions

In conclusion, our synthesis of $\text{Ho}^{3+}/\text{Er}^{3+}/\text{Yb}^{3+}$ and $\text{Nd}^{3+}/\text{Er}^{3+}/\text{Yb}^{3+}$ tri-doped $\text{Ba}_2\text{GdV}_3\text{O}_{11}$ phosphors using the sol-gel method has proven successful. The crystalline structure, affirmed by XRD results and Rietveld refinement analysis, reveals a monoclinic phase with $P2_1/c$ space group symmetry. These phosphors showcase a dual-mode temperature sensing mechanism, capitalizing on the temperature-dependent FIR responses linked to the $^2H_{11/2} \rightarrow ^4I_{15/2}$ (Er^{3+}) and the $^5S_{2/5}F_4 \rightarrow ^5I_8$ (Ho^{3+}) + $^4S_{3/2} \rightarrow ^4I_{15/2}$ (Er^{3+}) transitions, related to the emission bands at 525 nm and 555 nm, respectively. Additionally, the fluorescence lifetime of $^4S_{3/2}$ in Er^{3+} contributes to the two temperature sensing modes. The introduction of Ho^{3+} amplifies the red emission, while Nd^{3+} enhances the green emission. Calculated color purity reaches 84 % and 99 % for $\text{Ho}^{3+}/\text{Er}^{3+}/\text{Yb}^{3+}$ and $\text{Nd}^{3+}/\text{Er}^{3+}/\text{Yb}^{3+}$ tri-doped $\text{Ba}_2\text{GdV}_3\text{O}_{11}$ phosphors, respectively, showcasing superior color purity in the latter. Maximal relative sensitivities using the FIR strategy are 1.03 % K⁻¹ (at 298 K) for $\text{Ho}^{3+}/\text{Er}^{3+}/\text{Yb}^{3+}$ and 1.07 % K⁻¹ (at 298 K) for $\text{Nd}^{3+}/\text{Er}^{3+}/\text{Yb}^{3+}$. Employing the FL strategy, these phosphors exhibit sensitivities of 0.146 % K⁻¹ (at 573 K) and 0.47 % K⁻¹ (at 298 K), respectively, with the highest thermal sensitivity achieved using $\text{Nd}^{3+}/\text{Er}^{3+}/\text{Yb}^{3+}$ tri-doped $\text{Ba}_2\text{GdV}_3\text{O}_{11}$ phosphors. The uncertainties in temperature measurements using the FIR and FL strategies consistently remain low, with δT values below 0.3 K across the entire temperature range. This underscores the remarkable accuracy of both phosphors, emphasizing their significance in the field of optical thermometry. The exceptional temperature sensitivity and minimal thermal uncertainty demonstrated by $\text{Ho}^{3+}/\text{Nd}^{3+}$, Er^{3+} , Yb^{3+} tri-doped phosphors position them as promising candidates for optical temperature sensing applications. Our research lays the foundation for an innovative framework for the advancement and exploration of multi-mode self-referencing optical temperature sensors in the future.

Data availability

Data will be made available on request.

CRediT authorship contribution statement

Ikhlas Kachou: Writing – review & editing, Writing – original draft, Visualization, Validation, Investigation, Data curation. **Kamel Saidi:** Writing – review & editing, Writing – original draft, Visualization, Investigation, Data curation, Conceptualization. **Utku Ekim:** Writing – original draft, Visualization, Investigation, Data curation. **Mohamed Dammak:** Writing – review & editing, Writing – original draft, Visualization, Validation, Supervision, Methodology, Investigation, Formal analysis, Data curation, Conceptualization. **Miray Çelikbilek Ersundu:** Writing – review & editing, Writing – original draft, Visualization, Validation, Supervision, Methodology, Investigation, Formal analysis, Conceptualization. **Ali Erçin Ersundu:** Writing – review & editing, Writing – original draft, Visualization, Validation, Supervision, Methodology, Investigation, Funding acquisition, Conceptualization.

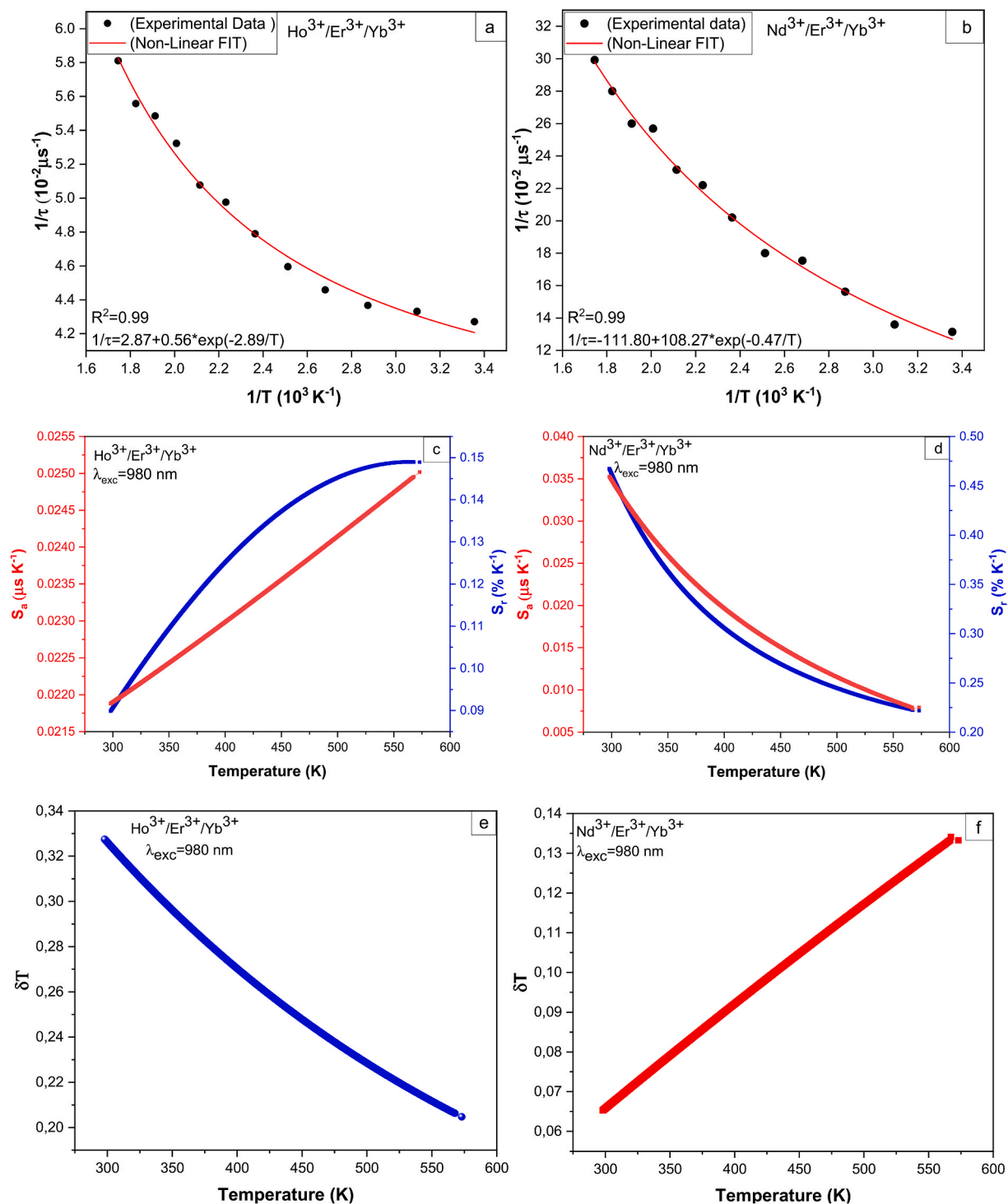


Fig. 14. (a), (b) Temperature dependency of the PL of $4S_{3/2}$ level of Er^{3+} average lifetime under 980 nm excitation, (c), (d) absolute and relative sensitivities calculated by FL, and (e), (f) the temperature uncertainty variations with temperature for $\text{Ho}^{3+}/\text{Er}^{3+}/\text{Yb}^{3+}$ and $\text{Nd}^{3+}/\text{Er}^{3+}/\text{Yb}^{3+}$ tri-doped $\text{Ba}_2\text{GdV}_3\text{O}_{11}$ phosphors, respectively.

Declaration of competing interest

The authors declare that they have no known competing financial interests or personal relationships that could have appeared to influence the work reported in this paper.

Table 2

Comparison of the maximum S_r and S_a parameters in $\text{Ho}^{3+}/\text{Er}^{3+}/\text{Yb}^{3+}$ and $\text{Nd}^{3+}/\text{Er}^{3+}/\text{Yb}^{3+}$ tri-doped $\text{Ba}_2\text{GdV}_3\text{O}_{11}$ phosphors using the FL strategy against various hosts.

Host	S_{amax} ($\mu\text{s K}^{-1}$)	S_{rmax} ($\% \text{K}^{-1}$)	T range (K)	$\lambda_{\text{exc}}/\lambda_{\text{dete}}$ (nm)	Reference
$\text{Y}_2\text{Mo}_4\text{O}_{15}:\text{Er}^{3+}/\text{Yb}^{3+}$	0.16 (520 K)	0.4 (520 K)	300–520	975/550	[65]
$\text{Ca}_2\text{MgWO}_6:\text{Er}^{3+}/\text{Yb}^{3+}$	0.12 (570 K)	0.11 (570 K)	300–570	980/549	[70]
$\text{Cs}_3\text{GdGe}_3\text{O}_9:\text{Er}^{3+}$	0.16 (313 K)	0.49 (313 K)	313–513	980/550	[67]
$\text{Na}_2\text{YMg}_2(\text{VO}_4)_3:\text{Er}^{3+}/\text{Yb}^{3+}$	0.0045 (368 K)	0.08 (412 K)	323–573	980/550	[71]
$\text{Cs}_2\text{Ag}_{0.6}\text{Na}_{0.4}\text{In}_{0.9}\text{Bi}_{0.1}\text{Cl}_2:\text{Er}^{3+}/\text{Yb}^{3+}$	0.0076 (300 K)	0.035 (300 K)	300–470	980/550	[72]
$\text{Ba}_2\text{GdV}_3\text{O}_{11}:\text{Ho}^{3+}/\text{Er}^{3+}/\text{Yb}^{3+}$	0.025 (573 K)	0.146 (573 K)	298–573	980/550	This work
$\text{Ba}_2\text{GdV}_3\text{O}_{11}:\text{Nd}^{3+}/\text{Er}^{3+}/\text{Yb}^{3+}$	0.036 (298 K)	0.47 (298 K)			

Appendix A. Supplementary data

Supplementary data to this article can be found online at <https://doi.org/10.1016/j.heliyon.2024.e30062>.

References

- H.-Q. Wang, M. Batentschuk, A. Osvet, L. Pinna, C.J. Brabec, Rare-earth ion doped up-conversion materials for Photovoltaic applications, *Adv. Mater.* 23 (22–23) (2011) 2675–2680, <https://doi.org/10.1002/adma.201100511>.
- Y. Tian, B. Tian, C. Cui, P. Huang, L. Wang, B. Chen, Size-dependent upconversion luminescence and temperature sensing behavior of spherical $\text{Gd}_2\text{O}_3:\text{Yb}^{3+}/\text{Er}^{3+}$ phosphor, *RSC Adv.* 5 (19) (2015) 14123–14128, <https://doi.org/10.1039/C4RA13204A>.
- R. Martín-Rodríguez, R. Valiente, S. Polizzi, M. Bettinelli, A. Speghini, F. Piccinelli, Upconversion luminescence in nanocrystals of $\text{Gd}_3\text{Ga}_5\text{O}_{12}$ and $\text{Y}_3\text{Al}_5\text{O}_{12}$ doped with $\text{Tb}^{3+}-\text{Yb}^{3+}$ and $\text{Eu}^{3+}-\text{Yb}^{3+}$, *J. Phys. Chem. C* 113 (28) (2009) 12195–12200, <https://doi.org/10.1021/jp901711g>.
- J. Zhou, Q. Liu, W. Feng, Y. Sun, F. Li, Upconversion luminescent materials: advances and applications, *Chem. Rev.* 115 (1) (2015) 395–465, <https://doi.org/10.1021/cr400478f>.
- B. Dong, B. Cao, Y. He, Z. Liu, Z. Li, Z. Feng, Temperature sensing and in vivo imaging by molybdenum sensitized visible upconversion luminescence of rare-earth oxides, *Adv. Mater.* 24 (15) (2012) 1987–1993, <https://doi.org/10.1002/adma.201200431>.
- J. Pichaandi, J.-C. Boyer, K.R. Delaney, F.C.J.M. van Veggel, Two-photon upconversion laser (scanning and wide-field) microscopy using Ln^{3+} -doped NaYF_4 upconverting nanocrystals: a critical evaluation of their performance and potential in bioimaging, *J. Phys. Chem. C* 115 (39) (2011) 19054–19064, <https://doi.org/10.1021/jp206345j>.
- K. Yamamoto, M. Fujii, S. Sowa, K. Imakita, K. Aoki, Upconversion luminescence of rare-earth-doped Y_2O_3 nanoparticle with metal nano-cap, *J. Phys. Chem. C* 119 (2) (2015) 1175–1179, <https://doi.org/10.1021/jp508443g>.
- I. Kachou, M. Dammak, S. Auguste, F. Amiard, P. Daniel, A novel optical temperature sensor and energy transfer properties based on $\text{Tb}^{3+}/\text{Sm}^{3+}$ codoped $\text{SrY}_2(\text{MoO}_4)_4$ phosphors, *Dalton Trans.* (2023), <https://doi.org/10.1039/D3DT03410K>.
- F. Zhang, G. Li, W. Zhang, Y.L. Yan, Phase-dependent enhancement of the green-emitting upconversion fluorescence in $\text{LaVO}_4:\text{Yb}^{3+}, \text{Er}^{3+}$, *Inorg. Chem.* 54 (15) (2015) 7325–7334, <https://doi.org/10.1021/acs.inorgchem.5b00851>.
- W. Zheng, P. Huang, D. Tu, E. Ma, H. Zhu, X. Chen, Lanthanide-doped upconversion nano-bioprobes: electronic structures, optical properties, and biodetection, *Chem. Soc. Rev.* 44 (6) (2015) 1379–1415, <https://doi.org/10.1039/C4CS00178H>.
- I. Kachou, K. Saidi, R. Salhi, M. Dammak, Synthesis and optical spectroscopy of $\text{Na}_3\text{Y}(\text{VO}_4)_2:\text{Eu}^{3+}$ phosphors for thermometry and display applications, *RSC Adv.* 12 (12) (2022) 7529–7539, <https://doi.org/10.1039/D2RA00539E>.
- Z.E.A.A. Taleb, K. Saidi, M. Dammak, D. Przybylska, T. Grzyb, Ultrasensitive optical thermometry using Tb^{3+} doped $\text{NaSrGd}(\text{MoO}_4)_3$ based on single band ratiometric luminescence, *Dalton Trans.* 52 (15) (2023) 4954–4963, <https://doi.org/10.1039/D3DT00376K>.
- D. Jia, Z. Yuan, H. San, L. Gao, The study of fluorescence thermal measurement based on DSP, *Procedia Eng.* 29 (2012) 2864–2868, <https://doi.org/10.1016/j.proeng.2012.01.405>.
- S. Balabhadra, M.L. Debasu, C.D.S. Brites, R.A.S. Ferreira, L.D. Carlos, Upconverting nanoparticles working as primary thermometers in different media, *J. Phys. Chem. C* 121 (25) (2017) 13962–13968, <https://doi.org/10.1021/acs.jpcc.7b04827>.
- M. Runowski, P. Woźny, I.R. Martín, V. Lavín, S. Lis, Praseodymium doped $\text{YF}_3:\text{Pr}^{3+}$ nanoparticles as optical thermometer based on luminescence intensity ratio (LIR) – studies in visible and NIR range, *J. Lumin.* 214 (2019) 116571, <https://doi.org/10.1016/j.jlumin.2019.116571>.
- K. Trejgis, L. Marciniak, The influence of manganese concentration on the sensitivity of bandshape and lifetime luminescent thermometers based on $\text{Y}_3\text{Al}_5\text{O}_{12}:\text{Mn}^{3+}, \text{Mn}^{4+}, \text{Nd}^{3+}$ nanocrystals, *Phys. Chem. Chem. Phys.* 20 (14) (2018) 9574–9581, <https://doi.org/10.1039/C8CP00558C>.
- M.G. Nikolić, Ž. Antić, S. Čulubrk, J.M. Nedeljković, M.D. Dramićanin, Temperature sensing with Eu^{3+} doped TiO_2 nanoparticles, *Sens. Actuators B Chem.* 201 (2014) 46–50, <https://doi.org/10.1016/j.snb.2014.04.108>.
- D. Wawrzynczyk, A. Bednarkiewicz, M. Nyk, W. Strek, M. Neodymium Samoc III, Doped fluoride nanoparticles as non-contact optical temperature sensors, *Nanoscale* 4 (22) (2012) 6959–6961, <https://doi.org/10.1039/C2NR32203J>.
- R.G. Geitenbeek, P.T. Prins, W. Albrecht, A. van Blaaderen, B.M. Weckhuysen, A. Meijerink, $\text{NaYF}_4:\text{Er}^{3+}, \text{Yb}^{3+}/\text{SiO}_2$ core/shell upconverting nanocrystals for luminescence thermometry up to 900 K, *J. Phys. Chem. C* 121 (6) (2017) 3503–3510, <https://doi.org/10.1021/acs.jpcc.6b10279>.
- B. Yalan, Z. Yunfei, Upconversion luminescence and optical thermometry of Pr^{3+} -doped KLu_2F_7 phosphor, *J. Mater. Sci. Mater. Electron.* 31 (10) (2020) 7991–7997, <https://doi.org/10.1007/s10854-020-03339-1>.
- W. Li, L. Hu, W. Chen, S. Sun, M. Guzik, G. Boulon, Enhanced red up-conversion of $\beta\text{-NaYF}_4:\text{Er}^{3+}, \text{Tm}^{3+}$ microcrystals for bio-imaging applications, *J. Alloys Compd.* 926 (2022) 166743, <https://doi.org/10.1016/j.jallcom.2022.166743>.
- K. Vignesh, D. Sivaganes, S. Saravanakumar, M.P. Rani, Ho³⁺-Induced ZnO: structural, electron density distribution and antibacterial activity for biomedical application, *Appl. Biochem. Biotechnol.* 195 (6) (2023) 3941–3965, <https://doi.org/10.1007/s12010-022-03865-0>.
- A. Nadort, J. Zhao, E.M. Goldys, Lanthanide upconversion luminescence at the nanoscale: fundamentals and optical properties, *Nanoscale* 8 (27) (2016) 13099–13130, <https://doi.org/10.1039/C5NR08477F>.
- L. Marciniak, A. Bednarkiewicz, Nanocrystalline NIR-to-NIR luminescent thermometer based on $\text{Cr}^{3+}, \text{Yb}^{3+}$ emission, *Sens. Actuators B Chem.* 243 (2017) 388–393, <https://doi.org/10.1016/j.snb.2016.12.006>.
- Y. Que, C. Feng, G. Lu, X. Huang, Polymer-coated ultrastable and biofunctionalizable lanthanide nanoparticles, *ACS Appl. Mater. Interfaces* 9 (17) (2017) 14647–14655, <https://doi.org/10.1021/acsami.7b01452>.

- [26] M. Runowski, N. Stopikowska, D. Szeremeta, S. Goderski, M. Skwierczyńska, S. Lis, Upconverting lanthanide fluoride Core@Shell nanorods for luminescent thermometry in the first and second biological windows: β -NaYF₄:Yb³⁺-Er³⁺@SiO₂ temperature sensor, *ACS Appl. Mater. Interfaces* 11 (14) (2019) 13389–13396, <https://doi.org/10.1021/acsami.9b00445>.
- [27] K. Saidi, M. Dammak, K. Soler-Carracedo, I.R. Martín, Optical thermometry based on upconversion emissions in Na₃Gd(VO₄)₂: Yb³⁺-Er³⁺/Ho³⁺ micro crystals, *J. Alloys Compd.* 891 (2022) 161993, <https://doi.org/10.1016/j.jallcom.2021.161993>.
- [28] P. Phogat, V.B. Taxak, S.P. Khatkar, R.K. Malik, Sm³⁺ incorporated Ba₂GdV₃O₁₁: photometric and crystal analysis of the ultraviolet triggered nanophosphor with white emission, *Chem. Phys.* 561 (2022) 111623, <https://doi.org/10.1016/j.chemphys.2022.111623>.
- [29] J. Dalal, M. Dalal, S. Devi, P. Dhankhar, A. Hooda, A. Khatkar, V.B. Taxak, S.P. Khatkar, Structural and Judd-Ofelt intensity parameters of a down-converting Ba₂GdV₃O₁₁:Eu²⁺ nanophosphors, *Mater. Chem. Phys.* 243 (2020) 122631, <https://doi.org/10.1016/j.matchemphys.2020.122631>.
- [30] P. Phogat, V.B. Taxak, R.K. Malik, Crystallographic and optical characteristics of ultraviolet-stimulated Dy³⁺-doped Ba₂GdV₃O₁₁ nanorods, *J. Electron. Mater.* 51 (8) (2022) 4541–4554, <https://doi.org/10.1007/s11664-022-09711-7>.
- [31] N. Kaczorowska, A. Szczesnak, S. Lis, Synthesis and tunable emission studies of new up-converting Ba₂GdV₃O₁₁ nanopowders doped with Yb³⁺/Ln³⁺ (Ln³⁺ = Er³⁺, Ho³⁺, Tm³⁺), *J. Lumin.* 200 (2018) 59–65, <https://doi.org/10.1016/j.jlumin.2018.03.085>.
- [32] P. Phogat, V.B. Taxak, R.K. Malik, Er³⁺ doped Ba₂GdV₃O₁₁: synthesis and characterization for crystal and photoluminescent features of bright green emitting nanophosphor, *Solid State Sci.* 133 (2022) 107013, <https://doi.org/10.1016/j.solidstatesciences.2022.107013>.
- [33] F. Ayachi, K. Saidi, M. Dammak, W. Chaabani, I. Mediavilla-Martínez, J. Jiménez, Dual-mode luminescence of Er³⁺/Yb³⁺ codoped LnP_{0.5}V_{0.5}O₄ (Ln=Y, Gd, La) for highly sensitive optical nanothermometry, *Mater. Today Chem.* 27 (2023) 101352, <https://doi.org/10.1016/j.mtchem.2022.101352>.
- [34] M. Runowski, P. Woźny, I.R. Martín, Optical pressure sensing in vacuum and high-pressure ranges using lanthanide-based luminescent thermometer-manometer, *J. Mater. Chem. C* 9 (13) (2021) 4643–4651, <https://doi.org/10.1039/D1TC00709B>.
- [35] P. Du, Y. Hou, W. Li, L. Luo, Ultra-high sensitivity of multicolor Sm³⁺-doped LiSrVO₄ phosphors for contactless optical thermometers, *Dalton Trans.* 49 (29) (2020) 10224–10231, <https://doi.org/10.1039/D0DT01907K>.
- [36] T. Wei, Y. Tian, C. Tian, M. Cai, X. Jing, B. Li, R. Chen, J. Zhang, S. Xu, Quantitative analysis of energy transfer and origin of quenching in Er³⁺/Ho³⁺ codoped germanosilicate glasses, *J. Phys. Chem. A* 119 (26) (2015) 6823–6830, <https://doi.org/10.1021/acs.jpca.5b04537>.
- [37] F. Ayachi, K. Saidi, W. Chaabani, M. Dammak, Synthesis and luminescence properties of Er³⁺ doped and Er³⁺-Yb³⁺ codoped phosphovanadate YP_{0.5}V_{0.5}O₄ phosphors, *J. Lumin.* 240 (2021) 118451, <https://doi.org/10.1016/j.jlumin.2021.118451>.
- [38] A.L. Moura, S.J. Carreño, P.I.R. Pincheira, L.J.Q. Maia, V. Jerez, E.P. Raposo, A.S.L. Gomes, C. B. de Araújo, Nonlinear effects and photonic phase transitions in Nd³⁺-doped nanocrystal-based random lasers, *Appl. Opt.* 59 (13) (2020) D155–D162, <https://doi.org/10.1364/AO.383477>.
- [39] R.S. Yadav, R.V. Yadav, A. Bahadur, S.B. Rai, Enhanced white light emission from a Tm³⁺/Yb³⁺/Ho³⁺ Co-doped Na₂ZnW₃O₁₂ nano-crystalline phosphor via Li⁺ doping, *RSC Adv.* 6 (57) (2016) 51768–51776, <https://doi.org/10.1039/C6RA08116A>.
- [40] D.L. Wood, J. Tauc, Weak absorption tails in amorphous semiconductors, *Phys. Rev. B* 5 (8) (1972) 3144–3151, <https://doi.org/10.1103/PhysRevB.5.3144>.
- [41] J. Tauc, R. Grigorovici, A. Vanco, Optical properties and electronic structure of amorphous germanium, *Phys. Status Solidi B* 15 (2) (1966) 627–637, <https://doi.org/10.1002/pssb.19660150224>.
- [42] Y. Liu, J. Silver, R.-J. Xie, J. Zhang, H. Xu, H. Shao, J. Jiang, H. Jiang, An excellent cyan-emitting orthosilicate phosphor for NUV-pumped white LED application, *J. Mater. Chem. C* 5 (47) (2017) 12365–12377, <https://doi.org/10.1039/C7TC04168C>.
- [43] G.D. Gesesse, A. Gomis-Berenguer, M.-F. Barthe, C.O. Ania, On the analysis of diffuse reflectance measurements to estimate the optical properties of amorphous porous carbons and semiconductor/carbon catalysts, *J. Photochem. Photobiol. Chem.* 398 (2020) 112622, <https://doi.org/10.1016/j.jphotochem.2020.112622>.
- [44] F. Ayachi, K. Saidi, K. Soler-Carracedo, M. Dammak, I.R. Martín, Coupled and non-coupled high sensitivity multi-mode ratiometric thermometry of Ho³⁺/Er³⁺/Yb³⁺ tri-doped YP_{0.5}V_{0.5}O₄ phosphors, *J. Alloys Compd.* 961 (2023) 171146, <https://doi.org/10.1016/j.jallcom.2023.171146>.
- [45] M. Wang, Y. Wu, F. Juan, Y. Li, B. Shi, F. Xu, J. Jia, H. Wei, B. Cao, Enhanced photocurrent of perovskite solar cells by dual-sensitized β -NaYF₄:Nd³⁺/Yb³⁺/Er³⁺ up-conversion nanoparticles, *Chem. Phys. Lett.* 763 (2021) 138253, <https://doi.org/10.1016/j.cplett.2020.138253>.
- [46] H. Liu, X. Jian, M. Liu, B. Wang, K. Wang, Y. Zhang, Constructing high sensitivity thermometry with dual-emitting Nd³⁺/Er³⁺/Yb³⁺ codoped BaWO₄ single crystal material, *Spectrochim. Acta. A. Mol. Biomol. Spectrosc.* 277 (2022) 121284, <https://doi.org/10.1016/j.saa.2022.121284>.
- [47] V. Mahalingam, J. Thirumalai, Effect of Co-doping of alkali metal ions on Ca_{0.5}RE_{1-x}(MoO₄)₂:xEu³⁺ (RE = Y, La) phosphors with enhanced luminescence properties, *RSC Adv.* 6 (84) (2016) 80390–80397, <https://doi.org/10.1039/C6RA16753E>.
- [48] M. Fhoula, T. Koubaa, M. Dammak, White photoluminescence and energy transfer properties of dysprosium and europium singly and codoped Na₂ZnP₂O₇ phosphors, *Opt. Laser Technol.* 130 (2020) 106352, <https://doi.org/10.1016/j.optlastec.2020.106352>.
- [49] K. Saidi, I. Kachou, K. Soler-Carracedo, M. Dammak, I.R. Martín, Ba₂YV₃O₁₁ Er³⁺/Yb³⁺ nanostructures for temperature sensing in the presence of bismuth ions, *ACS Appl. Nano Mater.* 6 (19) (2023) 17681–17690, <https://doi.org/10.1021/acsanm.3c02911>.
- [50] T. Ragin, A. Baranowska, M. Soltys, A. Górny, M. Kochanowicz, J. Zmojda, P. Miluski, R. Jadač, D. Dorosz, Intense and wide mid-infrared luminescence in bismuth-germanate glass Co-doped with Ho³⁺/Er³⁺/Yb³⁺ ions, *Infrared Phys. Technol.* 92 (2018) 139–143, <https://doi.org/10.1016/j.infrared.2018.06.003>.
- [51] X. Zhang, C. Zhang, S. Lai, Investigation of intense mid-infrared emission in Ho³⁺/Yb³⁺/Er³⁺ triple-doped tellurite glass, *Opt. Eng.* 61 (10) (2022) 106105, <https://doi.org/10.1117/1.OE.61.10.106105>.
- [52] M. Mondal, V.K. Rai, Optical thermometry using Stark sublevels in charge compensated transition metal molybdate upconverting phosphors, *Opt. Laser Technol.* 130 (2020) 106341, <https://doi.org/10.1016/j.optlastec.2020.106341>.
- [53] M. Mondal, V.K. Rai, Multiple ratiometric thermometry: enhanced sensing behaviour via Stark sublevels, *J. Alloys Compd.* 844 (2020) 155914, <https://doi.org/10.1016/j.jallcom.2020.155914>.
- [54] X. Li, L. Wang, J. Shi, N. Du, G. He, Multishelled nickel-cobalt oxide hollow microspheres with optimized compositions and shell porosity for high-performance pseudocapacitors, *ACS Appl. Mater. Interfaces* 8 (27) (2016) 17276–17283, <https://doi.org/10.1021/acsami.6b04654>.
- [55] G. Xiang, M. Xiong, Z. Yang, Y. Wang, L. Yao, S. Jiang, X. Zhou, L. Li, X. Wang, J. Zhang, Multipath optical thermometry realized by electronic levels and Stark sublevels of Er³⁺, *Ceram. Int.* (2023) <https://doi.org/10.1016/j.ceramint.2023.11.274>.
- [56] S.A. Wade, S.F. Collins, G.W. Baxter, Fluorescence intensity ratio technique for optical fiber point temperature sensing, *J. Appl. Phys.* 94 (8) (2003) 4743–4756, <https://doi.org/10.1063/1.1606526>.
- [57] V.K. Rai, Temperature sensors and optical sensors, *Appl. Phys. B* 88 (2) (2007) 297–303, <https://doi.org/10.1007/s00340-007-2717-4>.
- [58] J. Hu, B. Duan, Y. Wu, Y. Li, F. Wang, C. Ding, W. Jin, Intense red upconversion luminescence and optical thermometry of a novel Yb³⁺/Er³⁺ Co-doped Ba₃Sc₂WO₉ phosphor, *Mater. Res. Bull.* 171 (2024) 122633, <https://doi.org/10.1016/j.materresbull.2023.122633>.
- [59] M. Runowski, A. Bartkowiak, M. Majewska, I.R. Martín, S. Lis, Upconverting lanthanide doped fluoride NaLuF₄:Yb³⁺-Er³⁺-Ho³⁺ - optical sensor for multi-range fluorescence intensity ratio (FIR) thermometry in visible and NIR regions, *J. Lumin.* 201 (2018) 104–109, <https://doi.org/10.1016/j.jlumin.2018.04.040>.
- [60] L. Li, C. Guo, S. Jiang, D.K. Agrawal, T. Li, Green up-conversion luminescence of Yb³⁺-Er³⁺ Co-doped CaLa₂ZnO₅ for optically temperature sensing, *RSC Adv.* 4 (13) (2014) 6391, <https://doi.org/10.1039/c3ra47264g>.
- [61] J. Zhang, Z. Hua, Effect of dopant contents on upconversion luminescence and temperature sensing behavior in Ca₃La₆Si₆O₂₄:Yb³⁺-Er³⁺/Ho³⁺ phosphors, *J. Lumin.* 201 (2018) 217–223, <https://doi.org/10.1016/j.jlumin.2018.04.063>.
- [62] D. Manzani, J. Petrucci, K. Nigoghossian, A.A. Cardoso, S.J.L. Ribeiro, A portable luminescent thermometer based on green up-conversion emission of Er³⁺/Yb³⁺ Co-doped tellurite glass, *Sci. Rep.* 7 (2017) 1–11.
- [63] K. Saidi, W. Chaabani, M. Dammak, Highly sensitive optical temperature sensing based on pump-power-dependent upconversion luminescence in LiZnPO₄:Yb³⁺-Er³⁺/Ho³⁺ phosphors, *RSC Adv.* 11 (49) (2021) 30926–30936, <https://doi.org/10.1039/D1RA06049J>.
- [64] X. Liu, R. Lei, F. Huang, D. Deng, H. Wang, S. Zhao, S. Xu, Dependence of upconversion emission and optical temperature sensing behavior on excitation power in Er³⁺/Yb³⁺ Co-doped BaMoO₄ phosphors, *J. Lumin.* 210 (2019) 119–127, <https://doi.org/10.1016/j.jlumin.2019.01.065>.

- [65] K. Saidi, C. Hernández-Álvarez, M. Runowski, M. Dammak, I.R. Martín, Ultralow pressure sensing and luminescence thermometry based on the emissions of $\text{Er}^{3+}/\text{Yb}^{3+}$ codoped $\text{Y}_2\text{Mo}_4\text{O}_{15}$ phosphors, *Dalton Trans.* (2023), <https://doi.org/10.1039/D3DT02613B>.
- [66] K. Soler-Carracedo, I.R. Martín, F. Lahoz, H.C. Vasconcelos, A.D. Lozano-Gorrín, L.L. Martín, F. Paz-Buclatin, $\text{Er}^{3+}/\text{Ho}^{3+}$ codoped nanogarnet as an optical FIR based thermometer for a wide range of high and low temperatures, *J. Alloys Compd.* 847 (2020) 156541, <https://doi.org/10.1016/j.jallcom.2020.156541>.
- [67] R. Wei, F. Lu, L. Wang, F. Hu, X. Tian, H. Guo, Splendid four-mode optical thermometry design based on thermochromic $\text{Cs}_3\text{GdGe}_3\text{O}_9:\text{Er}^{3+}$ phosphors, *J. Mater. Chem. C* 10 (2022) 9492–9498, <https://doi.org/10.1039/D2TC01812H>.
- [68] H. Zhang, Y. Liang, H. Yang, S. Liu, H. Li, Y. Gong, Y. Chen, G. Li, Highly sensitive dual-mode optical thermometry in double-perovskite oxides via $\text{Pr}^{3+}/\text{Dy}^{3+}$ energy transfer, *Inorg. Chem.* 59 (19) (2020) 14337–14346, <https://doi.org/10.1021/acs.inorgchem.0c02118>.
- [69] C.D.S. Brites, A. Millán, L.D. Carlos, Chapter 281 - lanthanides in luminescent thermometry, in: B. Jean-Claude, K.P. Vitalij (Eds.), *Handbook on the Physics and Chemistry of Rare Earths*, vol. 49, Elsevier, 2016, pp. 339–427, <https://doi.org/10.1016/bs.hpcr.2016.03.005>. Including Actinides.
- [70] Y. Jiang, Y. Tong, S. Chen, W. Zhang, F. Hu, R. Wei, H. Guo, A three-mode self-referenced optical thermometry based on up-conversion luminescence of $\text{Ca}_2\text{MgWO}_6:\text{Er}^{3+}, \text{Yb}^{3+}$ phosphors, *Chem. Eng. J.* 413 (2021) 127470, <https://doi.org/10.1016/j.cej.2020.127470>.
- [71] Y. Tong, W. Zhang, R. Wei, L. Chen, H. Guo, $\text{Na}_2\text{YMg}_2(\text{VO}_4)_3:\text{Er}^{3+}, \text{Yb}^{3+}$ phosphors: up-conversion and optical thermometry, *Ceram. Int.* 47 (2) (2021) 2600–2606, <https://doi.org/10.1016/j.ceramint.2020.09.106>.
- [72] H. Xu, J. Yu, Q. Hu, Q. Han, W. Wu, Highly sensitive dual-mode optical thermometry of $\text{Er}^{3+}/\text{Yb}^{3+}$ codoped lead-free double perovskite microcrystal, *J. Phys. Chem. Lett.* 13 (4) (2022) 962–968, <https://doi.org/10.1021/acs.jpcclett.1c04000>.